A ciliopathy complex builds distal appendages to initiate ciliogenesis

Dhivya Kumar[1], Addison Rains[2], Vicente Herranz-Pérez[3,4] , Quanlong Lu[11], Xiaoyu Shi[5,6], Danielle L. Swaney[8,9,10], Erica Stevenson[8,9,10], Nevan J. Krogan[8,9,10] , Bo Huang[5,7], Christopher Westlake[11], Jose Manuel Garcia-Verdugo[3], Bradley Yoder[2] and Jeremy F. Reiter[1,7]

[1]Department of Biochemistry and Biophysics, Cardiovascular Research Institute, University of California, San Francisco, San Francisco, CA, USA

[2]Department of Cell, Developmental, and Integrative Biology, University of Alabama, Birmingham

[3]Laboratory of Comparative Neurobiology, Cavanilles Institute of Biodiversity and Evolutionary Biology, University of Valencia, CIBERNED, 46980 Valencia, Spain

[4]Predepartamental Unit of Medicine, Faculty of Health Sciences, Universitat Jaume I, 12071 Castelló de la Plana, Spain

[5]Department of Pharmaceutical Chemistry, University of California, San Francisco, San Francisco, CA 94143 USA

[6]Department of Developmental and Cell Biology, University of California Irvine, Irvine, CA 92697 USA

[7]Chan Zuckerberg Biohub, San Francisco, CA 94158, USA

[8]Department of Cellular and Molecular Pharmacology, University of California, San Francisco, San Francisco, CA 94158, USA

[9]California Institute for Quantitative Biosciences, QBI, University of California, San Francisco, San Francisco, CA 94158, USA

[10]J. David Gladstone Institutes, San Francisco, CA 94158, USA

[11]Center for Cancer Research, NCI Frederick, Laboratory of Cellular and Developmental Signaling, Frederick, MD 21702, USA.

*Correspondence: Jeremy.Reiter@ucsf.edu

Running Title: A distal centriole complex supports ciliogenesis

eTOC summary: Kumar et al. identifies a multi-protein complex called DISCO (DIStal centriole COmplex) required to nucleate distal appendages and restrain centriole elongation, essential for the initiation of cilium assembly. Without DISCO, cells fail to ciliate and transduce Hedgehog signals, critical for mammalian development.

ABSTRACT

Cells inherit two centrioles, the older of which is uniquely capable of generating a cilium. Using proteomics and super-resolved imaging, we identified a module which we term DISCO (DIStal centriole COmplex). DISCO components CEP90, MNR and OFD1 underlie human ciliopathies. This complex localized to both distal centrioles and centriolar satellites, proteinaceous granules surrounding centrioles. Cells and mice lacking CEP90 or MNR did not generate cilia, failed to assemble distal appendages, and did not transduce Hedgehog signals. Disrupting the satellite pools did not affect distal appendage assembly, indicating that it is the centriolar populations of MNR and CEP90 that are critical for ciliogenesis. CEP90 recruited the most proximal known distal appendage component, CEP83, to root distal appendages formation, an early step in ciliogenesis. In addition, MNR, but not CEP90, restricted centriolar length by recruiting OFD1. We conclude that DISCO acts at the distal centriole to support ciliogenesis by restraining centriole length and assembling distal appendages, defects in which cause human ciliopathies.

KEYWORDS: mother centriole, distal appendages, expansion microscopy, centriole length, centriolar satellites, DISCO

INTRODUCTION

Centrioles are ancient, microtubule-based structures with two main functions: first, they are core components of the centrosome, the primary microtubule organizing center, and, second, they are the foundations for cilia, cellular antennae specialized for signaling. While the main barrel of each centriole is comprised of nine radially arranged microtubule triplets, many proteins apart from tubulin comprise the centrioles (Winey and O'Toole, 2014; Keller et al., 2005, 2009; Jakobsen et al., 2011; Andersen et al., 2003). To date, the parts list of centrioles is incomplete.

Centriole structure can vary between species, but within a particular cell type, centriole length is nearly uniform, as are centriolar number and timing of assembly (Goehring and Hyman, 2012; Kong et al., 2020). Coordination with the cell cycle entrains this uniformity: centrioles duplicate during interphase and, at mitosis, each daughter cell inherits an older, mother centriole and a younger, daughter centriole (Nigg and Holland, 2018; Breslow and Holland, 2019).

The differences in centriolar age dictates different structures and functions. Only the mother centriole can assemble a cilium, and only it possesses subdistal and distal appendages. Through the distal appendages, the mother centriole attaches to pre-ciliary vesicles, an early step in ciliogenesis (Tanos et al., 2013; Sillibourne et al., 2013; Schmidt et al., 2012b). In contrast, sub-distal appendages are dispensable for ciliogenesis (Tanos et al., 2013; Mazo et al., 2016; Chong et al., 2020). Although components of appendages have been identified (Bowler et al., 2019; Yang et al., 2018; Chong et al., 2020), how they are assembled remains enigmatic.

Related to their roles in fundamental cellular processes such as cell division and intercellular communication, centriole dysfunction causes diverse human developmental disorders including ciliopathies and microcephaly (Nigg and Holland, 2018; Reiter and Leroux, 2017). For example, mutations in *CEP90* (*Centrosomal protein of 90 kDa*, also known as *PIBF1*), *MNR* (*MOONRAKER*, also known as *KIAA0753* or *OFIP*) or *OFD1* cause Joubert syndrome (JBTS), a ciliopathy characterized by brainstem and cerebellar malformations (Wheway et al., 2015; Shen et al., 2020; Hebbar et al., 2018; Stephen et al., 2017; Hammarsjö et al., 2017; Coene et al., 2009). Similarly, in many cancers, the number or structure of centrioles is dysregulated (Gönczy, 2015; Marteil et al., 2018).

CEP90 has been identified as a component of centriolar satellites, protein assemblies that orbit the centrosome (Kim et al., 2012; Kodani et al., 2015). Knockdown of *CEP90* alters the localization of centriolar satellites, which has been proposed to compromise ciliogenesis (Kim and Rhee, 2011; Kim et al., 2012).

We have used a combination of label retention expansion microscopy and structured illumination microscopy (LR-ExSIM) (Shi et al., 2019) and found that, in addition to being a component of centriolar satellites, CEP90 is a component of the distal end of centrioles. Proteomic analyses revealed that CEP90 is part of an evolutionarily conserved complex, which we term DISCO (DIStal centriole COmplex) that includes MNR and OFD1. Mouse genetic studies revealed that CEP90 and MNR are key regulators of mother centriole function, essential for normal vertebrate development, Hedgehog signaling and ciliogenesis. In investigating how CEP90 and MNR function in ciliogenesis, we found that both are required for the assembly of distal appendages. Mutant analysis demonstrated that the components of this distal centriole complex are recruited to the centriole in a hierarchical manner, culminating in CEP90, which recruits the most proximal distal appendage protein, CEP83, to initiate distal appendage formation. Thus, our work identifies an evolutionarily conserved complex that functions at the distal mother centriole to build distal appendages, an early and critical step in ciliogenesis.

RESULTS

CEP90 localizes to centriolar satellites and a ring at the distal ends of centrioles

CEP90 has previously been identified as a component of centriolar satellites (Kim and Rhee, 2011). We confirmed that CEP90 localizes to centriolar satellites by immunostaining human retinal pigment epithelial (RPE1) cells with antibodies to CEP90 and PCM1, a marker of centriolar satellites (Fig. 1a). In addition, a centrosomal pool of CEP90 did not co-localize with PCM1 (Fig. 1a). To more precisely identify where centrosomal CEP90 localized, we dispersed centriolar satellites with nocodazole and found that CEP90 localized with γ-tubulin at centrioles (Fig. 1b). Three-dimensional structured illumination microscopy (3D-SIM) revealed that CEP90 forms rings at centrioles (Fig. 1b).

Independent of nocodazole, we disrupted centriolar satellites in RPE1 cells by deleting PCM1, a scaffold for centriolar satellites, using CRISPR/Cas9 (Supplementary Fig 1). As described previously, centriolar satellites were not detected in *PCM1*$^{-/-}$ RPE1 cells (Odabasi et al., 2019). Consistent with the loss of satellites, localization of CEP90 to puncta around the centrosome was absent in *PCM1*$^{-/-}$ RPE1 cells (Fig. 1c). As in nocodazole-treated cells, the rings of CEP90 at centrioles remained in *PCM1*$^{-/-}$ RPE1 cells (Fig. 1c), indicating that CEP90 localizes to centrioles independently of PCM1 and centriolar satellites. To confirm antibody staining specificity, we immunostained exogenously expressed eYFP-tagged CEP90 in nocodazole-treated *PCM1*$^{-/-}$ RPE1 cells (Fig. 1d). Localization of eYFP-CEP90 resembled endogenous

135 CEP90 staining, and suggested that CEP90, unlike Centrobin and CEP164, localized to both
136 mother and daughter centrioles with similar fluorescence intensity (Fig. 1e).
137 Expansion microscopy involves physically expanding samples embedded in a hydrogel
138 (Wassie et al., 2019). To precisely map the localization of CEP90 at centrioles, we combined
139 expansion microscopy together with multi-color label retention and SIM (LR-ExSIM) to minimize
140 signal loss during expansion and provide ~30 nm lateral resolution (Shi et al., 2019). The distal
141 appendage component CEP164 imaged by LR-ExSIM was comparable to data previously
142 obtained using STORM: CEP164 formed a discontinuous ring at the mother centriole (Shi et al.,
143 2019, 2017). Intriguingly, LR-ExSIM resolved that the ring of CEP90 is comprised of discrete
144 puncta with a mode of nine and separated by a mean angle of ~ 36 nm (Fig. 1f-i). In agreement
145 with 3D-SIM microscopy, the CEP90 ring at the mother centriole as observed by LR-ExSIM had
146 a smaller diameter (228 ± 23 nm) and was proximal to the distal appendages. Thus, CEP90
147 comprises a nine-fold ring at the distal centriole (Fig 1j).
148
149 **CEP90, OFD1 and MNR form a distal centriole complex**
150 To gain insight into the function of CEP90 at the distal centriole, we proteomically identified
151 CEP90 interactors. More specifically, we generated RPE1 cell lines stably expressing GFP
152 (control) or YFP-CEP90. To discriminate proteins interacting with CEP90 at centriolar satellites
153 and those interacting with CEP90 at centrioles, we also generated *PCM1*$^{-/-}$ RPE1 cell lines stably
154 expressing GFP or YFP-CEP90 in which centriolar satellites are disrupted (Fig. 2a). We
155 immunoprecipitated GFP from these cell lines and detected co-immunoprecipitating proteins by
156 LC/MS/MS. Significance analysis of interactome (SAINTexpress (Teo et al., 2014)) analysis with
157 Bayesian false discovery rate (BFDR) < 0.05 indicated high confidence interactors (Fig. 2b and
158 c). Some CEP90 interactors, such as PCM1, CEP131 and BBS4, were identified in wild type cells,
159 but not in *PCM1*$^{-/-}$ cells, suggesting that these interactions are dependent on centriolar satellites.
160 Consistent with this conclusion, many of these PCM1-dependent interactors, including CEP131
161 and BBS4, are components of centriolar satellites (Hori and Toda, 2017).
162 To identify centriolar interactors of CEP90, we assessed which interactors were detected
163 in both WT and *PCM1*$^{-/-}$ RPE1 cells, as these interactions are predicted to be independent of
164 centriolar satellites. Notably, OFD1 and MNR, previously described components of centriolar
165 satellites and centrosomes that interact with each other (Chevrier et al., 2016), were detected as
166 CEP90 interactors (Fig. 2b and c). Using co-immunoprecipitation, we confirmed that CEP90
167 interacts with PCM1, MNR and OFD1 (Fig. 2d). Phylogenetic analysis revealed that CEP90, MNR

168 and OFD1 are largely co-conserved in metazoans, but absent in ecdysozoa such as *Drosophila*
169 *melanogaster* and *Caenorhabditis elegans* (Fig. 2e).
170 To assess whether MNR and OFD1 co-localize with CEP90, we immunostained RPE1
171 cells. CEP90 co-localized with MNR at centriolar satellites (Fig. 3a), and in cells treated with
172 nocodazole to disperse centriolar satellites, at centrioles (Fig. 3b). Similarly, MNR and OFD1 co-
173 localized at centriolar satellites (Fig. 3c), and centrioles in nocodazole treated cells (Fig. 3d). Thus,
174 like CEP90 and OFD1, MNR is a component of both centriolar satellites and centrioles.
175 To gain insight into the spatial organization of distal centriole proteins with respect to distal
176 appendages, we analyzed radially oriented centrioles with 3D-SIM (Fig. 3e). Consistent with
177 previous observations, distal appendage components CEP164 and CEP83 were organized into
178 respectively larger and smaller rings at the mother centriole (Yang et al., 2018; Bowler et al.,
179 2019). Of the distal centriole proteins, MNR was organized into the smallest ring (244 ± 29 nm)
180 (Fig. 3e and 3f). Talpid3, OFD1 and CEP90 also were organized into rings that, intriguingly, were
181 of different diameters at the mother and daughter centrioles. At the mother centriole, rings, from
182 largest to smallest, were comprised of Talpid3 (345 ± 27 nm), OFD1 (317 ± 37 nm) and CEP90
183 (291 ± 35 nm). At the daughter centriole, these rings were smaller and ordered differently from
184 largest to smallest as OFD1 (288 ± 21 nm), CEP90 (263 ± 21 nm) and Talpid3 (255 ± 24 nm) (Fig.
185 3e and 3f), indicating that the distal centriole is reorganized when the daughter centriole matures
186 into a mother.
187 Centriole biogenesis is coordinated with the cell cycle. Procentrioles form during S phase
188 and elongate in G2. To ascertain when distal centriole proteins are recruited to centrioles, we
189 used EdU incorporation and CENPF staining to distinguish between cells in different stages of
190 the cell cycle (Viol et al., 2020). CEP90, OFD1 and MNR localized to mother and daughter
191 centrioles in cells in G1 (EdU negative, CENPF negative) and in S phase (EdU positive, CENPF
192 negative) (Fig. 3g). In G2 (EdU negative, CENPF positive), both centrosomes (marked by γ-
193 tubulin) each possessed two puncta of CEP90, OFD1 and MNR (Fig. 3g). Therefore, CEP90,
194 OFD1 and MNR are recruited to the distal end of elongating procentrioles in G2.
195
196 **CEP90 and MNR are critical for vertebrate development, ciliogenesis and Hedgehog**
197 **signaling**
198 To assess the function of CEP90 and MNR, we generated RPE1 cell lines lacking CEP90
199 and MNR using CRISPR/Cas9. Immunoblot analyses confirmed loss of protein in the mutant cell
200 lines (Supplementary Fig 1 a-d). Notably, *CEP90*$^{-/-}$ and *MNR*$^{-/-}$ RPE1 cells possess centrioles but
201 both lacked cilia (Fig. 4a and 4b). As we previously identified a role for OFD1 in cilium assembly

202 (Singla et al., 2010; Hunkapiller et al., 2011), we conclude that the CEP90, MNR, OFD1 distal
203 centriole complex is essential for ciliogenesis.
204 To query the function of CEP90 and MNR in vertebrates, we obtained *Cep90* and *Mnr*
205 mutant mice from IMPC. The *Cep90* mutant mice (*Pibf1*$^{tm1.1\ (KOMP)Vlcg}$) contain a deletion of 7 exons,
206 and the *Mnr* mutant mice (*4933427D14Rik*$^{tm1\ (KOMP)Vlcg}$) contain a deletion of 10 exons.
207 Heterozygous *Cep90* and *Mnr* mice were viable and fertile, with no obvious phenotypes.
208 Homozygous *Cep90* and *Mnr* mice did not survive beyond embryonic day (E) 9.5. At E9.5, *Cep90*$^{-}$
209 $^{/-}$ and *Mnr*$^{-/-}$ embryos displayed pericardial edema (Fig. 4c) and unlooped, midline hearts. One key
210 role for primary cilia is in transducing extracellular signals including Hedgehog proteins, secreted
211 morphogens required for vertebrate development. As lack of Smoothened, a central component
212 of the Hedgehog signal transduction pathway, or lack of cilia also produces unlooped, midline
213 hearts (Corbit et al., 2005; Huangfu et al., 2003), we examined the presence of cilia in *Cep90*$^{-/-}$
214 and *Mnr*$^{-/-}$ embryos. γ-tubulin-positive centrioles were detected in both wild type and *Cep90*$^{-/-}$
215 embryonic nodes at E8.5, but cilia were absent from *Cep90*$^{-/-}$ nodes (Fig. 4d). Consistent with a
216 defect in ciliogenesis, *Cep90*$^{-/-}$ embryos also displayed attenuated expression of the Hedgehog
217 target gene, *Gli1*, indicating defects in Hedgehog signal transduction (Fig. 4e). Similarly, cilia
218 detected by ARL13B staining were absent in neural tube sections from E9.5 *Mnr*$^{-/-}$ embryos (Fig.
219 4f). Mouse embryonic fibroblasts (MEFs) derived from *Cep90*$^{-/-}$ and *Mnr*$^{-/-}$ embryos recapitulated
220 the ciliogenesis phenotype observed in *CEP90*$^{-/-}$ and *MNR*$^{-/-}$ RPE1 cells (Fig. 4g, h, j, k).
221 Furthermore, qRT-PCR analysis confirmed that induction of Hedgehog target genes, *Gli1* and
222 *Ptch1,* in response to the Hedgehog pathway agonist SAG was abrogated in *Cep90*$^{-/-}$ and *Mnr*$^{-/-}$
223 MEFs (Fig. 4 i, l). Thus, CEP90 and MNR are both required for vertebrate development,
224 ciliogenesis, and Hedgehog signaling.
225
226 **CEP90 ciliopathy mutations affect ciliogenesis and centriolar satellite morphology**
227 To identify regions in CEP90 required for cilium assembly, we tested whether CEP90
228 lacking either the N-terminus, C-terminus or central domain (Kim et al., 2012) could support
229 ciliogenesis in *CEP90*$^{-/-}$ RPE1 cells (Fig. 5a). Unlike expression of the full length CEP90 (FL-
230 CEP90), CEP90 lacking the N terminal (CEP90$^{363-757}$) or the C-terminal (CEP90$^{1-363}$) regions failed
231 to rescue ciliogenesis defects in *CEP90*$^{-/-}$ RPE1 cells (Fig.5b,c). A construct of CEP90 lacking
232 residues required for interaction with PCM1 (CEP90$^{\Delta 271-363}$) localized to the centrosomal region,
233 and partially rescued ciliogenesis defects in *CEP90*$^{-/-}$ RPE1 cells (Fig. 5a-c). These data support
234 a role for both N and C-terminal regions of CEP90 in ciliogenesis, further highlighting its function
235 as a critical centriolar scaffold.

236 We also examined whether disease-associated variants of CEP90 compromise its ability to
237 support cilia assembly or centriolar satellite localization. Previously, we identified a rare variant in
238 CEP90 (CEP90^{E89Q}) associated with microcephaly (Kodani et al., 2015). Surprisingly, this variant
239 of CEP90 displayed normal localization to centrioles and centriolar satellites (Fig. 5c), but failed
240 to support ciliogenesis in *CEP90*$^{-/-}$ RPE1 cells (Fig. 5b,c). We also assessed two mutant forms of
241 CEP90 (CEP90^{R405Q} and CEP90^{D637A}) implicated in Joubert syndrome (Wheway et al., 2015)
242 (Fig.5b,c). Interestingly, both Joubert associated variants of CEP90 perturbed centriolar satellite
243 morphology (Fig. 5c), and showed reduced ability to support ciliogenesis in *CEP90*$^{-/-}$ RPE1 (Fig.
244 5b). Thus, our data suggest that distinct human disease-associated mutations in *CEP90*
245 differentially compromise centriolar satellite morphogenesis and ciliogenesis.
246 To identify regions of CEP90 required for interaction with DISCO components, OFD1 and
247 MNR, we performed co-immunoprecipitation experiments with CEP90 truncation constructs. Both
248 OFD1 and MNR preferentially interacted with the C-terminal region of CEP90 (CEP90$^{363-757}$),
249 CEP90 lacking the C-terminal (CEP90$^{1-363}$) failed to immunoprecipitate OFD1 and MNR (Fig 5d-
250 g). Therefore, the C-terminal region of CEP90 (in which mutations cause Joubert syndrome) is
251 critical for interaction with DISCO subunits, OFD1 and MNR (Wheway et al., 2015).
252
253 **MNR, but not CEP90, restricts centriolar length**
254 Since distal centriole proteins OFD1, Talpid3 and C2CD3 control centriole length, we
255 analyzed *CEP90*$^{-/-}$ and *MNR*$^{-/-}$ centrioles labeled with Tubulin^{Ac} and distal centriole protein
256 CEP162 by 3D-SIM. Compared to control centrioles, centriole length was not altered in *CEP90*$^{-/-}$
257 cells. However, centriole length was highly variable in *MNR*$^{-/-}$ cells, with ~30% of *MNR*$^{-/-}$ cells
258 containing hyper-elongated centrioles (some of which were over a micron long, Fig 6. a-c). The
259 hyper-elongated centrioles in *MNR*$^{-/-}$ cells possessed the distal centriole component CEP162 at
260 one end, suggesting that proximal-distal polarity is maintained despite the elongation (Fig. 6 a).
261 Serial section transmission electron microscopy (TEM) analysis confirmed the presence of
262 elongated centrioles in *MNR*$^{-/-}$ RPE1 cells (Fig. 6 d-e). Both mother and daughter centrioles
263 (distinguished by localization of Ninein to the mother centriole-specific sub-distal appendage)
264 were hyper-elongated in *MNR*$^{-/-}$ cells (Fig. 6f). Therefore, MNR restrains centriole lengthening of
265 both mother and daughter centrioles (Fig. 6f-g).
266 The abnormal centriole morphology in *MNR*$^{-/-}$ cells is reminiscent of the phenotype we
267 previously observed in *OFD1* mutant cells (Singla et al., 2010). Therefore, we examined the
268 localization of OFD1 in *MNR*$^{-/-}$ RPE1 cells. OFD1 failed to localize to the centrioles in the absence
269 of MNR, but not CEP90 (Fig. 6 h-i). Overexpressed MNR localizes to microtubules (Chevrier et

270 al., 2016) and microtubule-associated MNR can sequester endogenous OFD1 (Supplementary
271 figure 2). Therefore, MNR is necessary and sufficient to recruit OFD1 (Fig. 6h-i), and our data
272 support a model in which MNR recruits OFD1 to restrict centriole length(Feng et al., 2017;
273 Srivastava and Panda, 2017), with CEP90 being dispensable for centriole length control and
274 dedicated to ciliogenesis.
275
276 **CEP90 and MNR are required for the removal of CP110 and CEP97 from the mother**
277 **centriole at the initiation of ciliogenesis**
278 Ciliogenesis depends on a specialized protein transport machinery called intraflagellar
279 transport (IFT). We examined whether IFT88 localization to basal bodies depends on CEP90 or
280 MNR, and found that IFT88 was decreased at the mother centriole of both *CEP90*$^{-/-}$ and *MNR*$^{-/-}$
281 RPE1 cells in both serum-starved (Fig. 7 a,b) and cycling cells (Supplementary Fig. 3a-b).
282 A critical early step in ciliogenesis is the removal from the distal mother centriole of two
283 proteins that can inhibit ciliogenesis, CP110 and CEP97. We tested whether CEP90 or MNR
284 function removal of CP110 and CEP97 by examining *CEP90*$^{-/-}$ and *MNR*$^{-/-}$ RPE1 cells. We found
285 that cells lacking either CEP90 or MNR fail to remove CP110 and CEP97 (Fig. 7c-f). Taken
286 together, these results reveal that CEP90 and MNR are required for early steps of ciliogenesis.
287
288 **CEP90 and MNR are required for ciliary vesicle docking and distal appendage assembly**
289 As ciliary vesicle formation contributes to removing CP110 and CEP97 from the mother
290 centriole (Westlake et al., 2011; Lu et al., 2015), we investigated whether persistence of CP110
291 and CEP97 in *CEP90*$^{-/-}$ and *MNR*$^{-/-}$ cells was due to defective recruitment of preciliary vesicles.
292 To assess whether CEP90 and MNR affect preciliary vesicle recruitment, we examined
293 the localization of Myosin-Va-positive preciliary vesicles (Wu et al., 2018) to centrioles in wild
294 type, *CEP90*$^{-/-}$ and *MNR*$^{-/-}$ RPE1 cells. Consistent with the defect in distal appendage formation,
295 cells lacking either CEP90 or MNR showed reduced Myosin-Va at the mother centriole (Fig. 7g-
296 h). To confirm the requirement for both CEP90 and MNR in preciliary vesicle recruitment, we
297 examined wild-type and knockout cells by serial section TEM, which confirmed that centrioles in
298 cells lacking CEP90 or MNR fail to dock to preciliary vesicles (Fig. 7i-j and Supplementary Figures
299 4). Thus, CEP90 and MNR are essential for ciliary vesicle recruitment to the mother centriole, a
300 key early step of ciliogenesis (Fig. 7k).
301 An early step of ciliogenesis is the acquisition of appendages by the mother centriole,
302 defining its maturation into a basal body. Sub-distal appendages mediate the anchoring of the
303 basal body to microtubules and regulate the spatial positioning of the cilium in the cell (Mazo et

304 al., 2016). In *CEP90*$^{-/-}$ and *MNR*$^{-/-}$ RPE1 cells, the localization of components of sub-distal
305 appendages, such as Ninein and CEP170, were unaffected (Supplementary Fig 5a-d), indicating
306 that CEP90 and MNR are dispensable for subdistal appendage formation.
307 A function of distal appendages is the recruitment of small preciliary vesicles to the mother
308 centriole which fuse and give rise to the ciliary membrane (Tanos et al., 2013; Schmidt et al.,
309 2012a). *CEP90*$^{-/-}$ and *MNR*$^{-/-}$ centrioles fail to recruit distal appendage proteins CEP83, FBF1,
310 SCLT1, ANKRD26 and CEP164, indicating that they are essential for distal appendage formation
311 (Fig. 8c-g). FBF1 and CEP164 failed to localize to the mother centriole in cycling *CEP90*$^{-/-}$ and
312 *MNR*$^{-/-}$ cells, indicating that CEP90 and MNR organize the distal appendage irrespective of
313 whether serum starvation initiates ciliogenesis (Supplementary Fig. 3e-h). CEP90 and MNR are
314 not critical for distal appendage protein abundance (Supplementary Fig 6e), suggesting that they
315 are not required for distal appendage protein stability but rather are essential for distal appendage
316 assembly at the mother centriole.
317 Recent studies show that daughter centriole proteins are removed from the mother centriole
318 to enable distal appendage assembly (Wang et al., 2018; Mahjoub et al., 2010). Since CEP90
319 localizes to the distal daughter centriole as well as the distal mother centriole, we hypothesized
320 that CEP90 may interact with distal daughter centriole proteins. Co-immunoprecipitation revealed
321 that CEP90 did interact with daughter centriole components Centrobin and CEP120
322 (Supplementary Fig. 5f). As removing daughter centriole proteins requires distal centriole
323 proteins, such as Talpid3, we examined the localization of Talpid3 and found that Talpid3 is
324 recruited to the distal centriole in both wild-type and *CEP90*$^{-/-}$ and *MNR*$^{-/-}$ RPE1 cells
325 (Supplementary Fig. 5g and h). Similarly, Centrobin and CEP120 localized to only one centriole
326 in both wild-type and *CEP90*$^{-/-}$ and *MNR*$^{-/-}$ RPE1 cells (Supplementary Fig. 5 i-l). Therefore,
327 CEP90 and MNR regulate distal appendage formation through a mechanism independent of
328 Talpid3 recruitment or daughter centriole protein removal.
329
330 **CEP90 functions at the mother centriole to support distal appendage formation**
331 Using siRNA-mediated gene knockdown, a previous study showed that CEP90 promotes
332 centriolar satellite accumulation in the vicinity of centrosomes. We confirmed that, in *CEP90*$^{-/-}$
333 RPE1 cells, PCM1- positive centriolar satellites failed to accumulate around centrosomes (Fig 9a
334 and 9b). Interestingly, loss of MNR did not affect targeting of PCM1- positive centriolar satellites
335 to the centrosome (Fig 9a and 9b), indicating that CEP90 and MNR have some distinct functions
336 in centriolar satellite distribution. These observations raised the interesting possibility that CEP90-

337 dependent targeting of centriolar satellites to the centrosomal area promotes distal appendage
338 formation and ciliogenesis.

339 As *PCM1*$^{-/-}$ cells lack centriolar satellites but retain CEP90 at centrioles (Fig. 1c), these
340 cells can help disentangle the functions of CEP90 and MNR at centriolar satellites and centrioles.
341 In accordance with previous observations (Wang et al., 2016; Odabasi et al., 2019), RPE1 cells
342 lacking PCM1 displayed compromised ciliogenesis (Fig 9c). In stark contrast to *CEP90*$^{-/-}$ cells,
343 distal appendage components CEP83, SCLT1and CEP164 localized equivalently to the mother
344 centrioles of *PCM1*$^{-/-}$ and wild type RPE1 cells (Fig 9d-i), indicating that distal appendage
345 assembly is independent of PCM1. Furthermore, serial section transmission electron microscopy
346 confirmed the presence of distal appendages in *PCM1*$^{-/-}$ RPE1 cells (Fig 9j). As the critical
347 centriolar satellite scaffold PCM1 is not required for either CEP90 localization to centrioles or
348 distal appendage formation, we conclude that the centriolar satellite population of CEP90 is
349 dispensable for distal appendage assembly.

350 If the centriolar satellite population is dispensable, we predicted that MNR and OFD1
351 recruitment of CEP90 to the distal centriole would be critical for distal appendage assembly and
352 ciliogenesis. Indeed, we found that although CEP90 protein levels were unchanged in *MNR*$^{-/-}$
353 RPE1 cells (Supplementary Fig. 1d), CEP90 failed to localize to *MNR*$^{-/-}$ centrioles, while MNR
354 localized to the centrioles in the absence of CEP90 (Fig. 10 a-d).

355 To investigate how CEP90 can be specifically required for the formation distal
356 appendages, we investigated whether CEP90 reorganizes distal centriole proteins at the mother
357 centriole to promote distal appendage assembly. 3D-SIM analysis revealed that Talpid3 and
358 OFD1 diameters were smaller in mother centrioles of *CEP90*$^{-/-}$ cells compared to WT (Fig 10e
359 and 10f). These results support a model where CEP90 functions in the transformation of a
360 daughter to a mother centriole by reorganizing the distal centriole.

361 Next, we examined whether CEP90 interacts with the distal centriole base. Co-
362 immunoprecipitation analysis revealed an interaction between CEP90 and the proximal most-
363 component of the distal centriole, CEP83 (Fig. 10g). We propose that MNR recruits CEP90 to the
364 distal centriole, and CEP90, in turn, recruits CEP83 to initiate distal appendage assembly (Fig.
365 10h). Therefore, distal centriolar proteins are recruited in a hierarchical manner, with MNR
366 recruiting OFD1 to restrict centriole length, and CEP90 dedicated to distal appendage assembly.
367

368 **DISCUSSION**

369 **CEP90 and MNR are critical for distal appendage assembly and ciliogenesis**

370 Through the process of mitosis, vertebrate daughter cells each inherit two centrioles. Yet,
371 only the older, mother centriole templates a cilium. In no small part, this unique function of the
372 mother centriole depends on its distal appendages, acquired during the previous G2/M phase. In
373 this study, we identify a multi-protein complex which we name DISCO, comprised of CEP90,
374 OFD1 and MNR and critical for distal appendage formation and ciliogenesis.
375 Consequent to their role in distal appendage formation, CEP90 and MNR are also required
376 for subsequent events in ciliogenesis, including recruitment of the preciliary vesicles that give rise
377 to the ciliary membrane, and loading of IFT88 (Sillibourne et al., 2013; Tanos et al., 2013). Unlike
378 some other centriolar proteins, such as CEP120 (Tsai et al., 2019), CEP90 and MNR are
379 specifically required for distal appendage formation, but dispensable for subdistal appendage
380 formation, revealing that discrete mother centriolar complexes support distal and subdistal
381 appendage assembly.
382 In mice, we found that CEP90 and MNR are essential for embryonic development, and
383 particularly for Hedgehog signaling. Primary cilia are required for Hedgehog signal transduction
384 in vertebrates. A central component of the Hedgehog pathway is the seven-pass transmembrane
385 protein, Smoothened (Smo). Interestingly, *Cep90, Mnr* and *Smo* mutants arrested at similar points
386 in embryonic development and displayed similar phenotypes, emphasizing the importance of
387 CEP90 and MNR in ciliary Hedgehog signaling.
388
389 **MNR recruits OFD1 to regulate centriole length**
390 CEP90 and MNR colocalize with their interactor OFD1 at the distal ends of centrioles. We
391 found that distal centriole proteins are recruited to the centriole in a hierarchical manner. MNR
392 forms the innermost ring at the distal centriole and is essential for the recruitment of OFD1 and
393 CEP90, whereas CEP90 is dispensable for the recruitment of the other complex members.
394 Overexpressed MNR localizes to microtubules (Chevrier et al., 2016) bringing along OFD1.
395 Therefore, we propose that MNR binds to the distal centriolar microtubules to recruit OFD1,
396 culminating in CEP90 recruitment (Fig. 10).
397 We had previously demonstrated that OFD1 was essential to restrain centriolar length
398 (Singla et al., 2010). We have found that one of its partners, MNR, is also critical to restrict
399 centriolar elongation. However, its other partner, CEP90, does not control centriolar length. Thus,
400 within the complex comprised of MNR, OFD1 and CEP90, the subunits have distinct functions,
401 with CEP90 dedicated to founding distal appendages. Consequently, the requirement for MNR
402 and OFD1 in distal appendage assembly may be secondary to their roles in recruiting CEP90 to
403 the distal centriole. The most parsimonious model is that MNR (and perhaps OFD1) at the distal

404 centriole recruits CEP90 to build distal appendages, and that MNR recruits OFD1 to restrict
405 centriole elongation.

406 **CEP90 recruits CEP83 to initiate distal appendage assembly at the mother centriole**

407 The functions of centriolar satellites, although intimately associated with centrosomes,
408 remain unclear (Odabasi et al., 2019; Prosser and Pelletier, 2020). CEP90 is a component of
409 centriolar satellites, where it interacts with PCM1, the major scaffolding protein of centriolar
410 satellites (Kim et al., 2012). Like CEP90, its interactors MNR and OFD1 are centriolar satellite
411 proteins. As loss of CEP90 disrupts the peri-centrosomal localization of centriolar satellites, we
412 initially hypothesized that centriolar satellites transport CEP90 to centrioles, or that CEP90 acts
413 at centriolar satellites to transport distal appendage components to the mother centriole. In *PCM1*$^{-}$
414 $^{/-}$ RPE1 cells, centriolar satellites are disrupted but CEP90 remains at the distal centriole,
415 indicating that satellites are dispensable for CEP90 localization at centrioles. Moreover, to our
416 surprise, we found that *PCM1*$^{-/-}$ RPE1 cells assemble distal appendages. Thus, centriolar
417 satellites (and CEP90 at centriolar satellites) are dispensable for distal appendage assembly,
418 indicating that CEP90 functions at the distal centriole to build distal appendages.

419 A combination of expansion and structured illumination super-resolution microscopy
420 revealed that CEP90 decorates the distal centriole in a discontinuous ring-like pattern with nine-
421 fold symmetry; this ring of CEP90 is proximal to and smaller than the ring of CEP164. While
422 antibodies to endogenous CEP90 label the daughter centriole more heavily than the mother
423 centriole, epitope-tagged CEP90 localizes equivalently to both the mother and daughter
424 centrioles. We speculate that reduced accessibility of the CEP90 antibody once distal
425 appendages are assembled at the mother centriole may limit endogenous CEP90
426 immunofluoresence.

427 At the centriole, CEP90 interacts with and is critical for the recruitment of the distal
428 appendage component CEP83. As CEP83 is the root of the distal appendage (Tanos et al., 2013),
429 CEP90 is required to initiate distal appendage formation. In support of this conclusion, no distal
430 appendage-like structures were observable in serial section transmission electron micrographs of
431 cells lacking CEP90. These data raise the tantalizing possibility that the nine-fold ring of CEP90
432 at the distal centriole templates the assembly of the distal appendages.

433 Super-resolved microscopy also revealed that OFD1 and Talpid3 are structurally different
434 in the mother and daughter centrioles, with the diameter of both rings increasing upon transition
435 from daughter to mother. CEP90 is essential for OFD1 and Talpid3 rings to dilate to the mother
436 centriole-specific diameter. We propose that this CEP90-dependent reorganization of distal
437 centriole directs adoption of mother centriole-specific properties, including distal appendage

438 assembly and ciliogenesis. Future work will focus on establishing how CEP90 reorganizes OFD1
439 and Talpid3 at the distal mother centriole to initiate distal appendage assembly.
440 In addition to MNR, OFD1 and CEP90, Talpid3 and C2CD3 localize to the distal centriole
441 and are required for distal appendage formation (Singla et al., 2010; Thauvin-Robinet et al., 2014;
442 Ye et al., 2014; Wang et al., 2018). We did not identify C2CD3 or Talpid3 in our proteomic
443 analysis, suggesting that they might be part of a distinct, distal centriole complex (Tsai et al.,
444 2019). Although CEP90 interacts with daughter centriole proteins CEP120 and Centrobin, Talpid3
445 recruitment, and the subsequent removal Centrobin and CEP120 from the distal mother centriole
446 occurs normally in *CEP90*$^{-/-}$ RPE1 cells. Therefore, CEP90 acts independently or downstream of
447 Talpid3 recruitment and daughter centriole protein removal to regulate distal appendage
448 assembly.
449 Mutations in *CEP90* cause Joubert syndrome (Kodani et al., 2015; Wheway et al., 2015;
450 Hebbar et al., 2018), while *OFD1* and *MNR* cause Orofaciodigital and Joubert syndrome (Singla
451 et al., 2010; Stephen et al., 2017; Chevrier et al., 2016; Coene et al., 2009). Joubert and
452 Orofaciodigital syndromes have partially overlapping clinical features. Ultrastructural studies have
453 identified a cogwheel-like structure at the distal domain of human centrioles (Paintrand et al.,
454 1992; Ibrahim et al., 2009), raising the possibility that DISCO may be components of this structure.
455 We propose that DISCO both controls centriolar length and builds distal appendages, and that
456 inherited defects in this cogwheel that compromise these critical functions attenuate ciliogenesis,
457 Hedgehog signaling and embryonic patterning, resulting in Joubert and Orofaciodigital
458 syndromes.
459

460 **MATERIAL AND METHODS**

461 **Mouse lines**

462 *Cep90* (*Pibf1*$^{tm1.1(KOMP)Vlcg}$) and *Mnr* (*4933427D14Rik*$^{tm1.1(KOMP)Vlcg}$) mice, generated in a
463 C57BL/6NJ background were obtained from the International Mouse Phenotyping Consortium.
464 Mice were housed in a barrier facility with veterinary supervision and given food and water *ad*
465 *libitum*. All mouse protocols were approved by the Institutional Animal Care and Use Committee
466 at the University of California, San Francisco and the University of Alabama, Birmingham.

467 **Cell lines and cell culture**

468 Human retinal epithelial (RPE1-hTERT) cells were cultured in DMEM/F12 (Thermo Fisher;
469 catalog 10565042) supplemented with 10 % FBS at 37 ºC in 5% CO_2. To induce ciliation, cells

470 were serum starved in Opti-MEM reduced serum media for indicated times. 293T cells were
471 cultured in DMEM supplemented with 10% FBS and 1X GlutaMAX at 37 ºC in 5% CO_2.

472 RPE1 cell lines stably expressing eYFP-CEP90 were generated using lentiviruses containing the
473 human *CEP90* cDNA (gift from Kunsoo Rhee (Kim and Rhee, 2011; Kim et al., 2012)) in the
474 pLVX-IRES-Puro (Clontech, Mountain View, CA) plasmid background. *CEP90*$^{-/-}$ RPE1 cells
475 expressing mNeonGreen-tagged full length, truncation and disease-associated mutation variants
476 of CEP90 were generated using lentiviruses containing human *CEP90* cDNA in a pLVX-EF1α$^{\Delta}$-
477 mNeonGreen plasmid background. Lentiviruses were generated using the Lenti-X Packaging
478 Single Shot system (Takara Bio), according to manufacturer's guidelines. Infected cells were
479 plated in a glass-bottom 96 well plate (Cellvis; catalog P96-1.5H-N) using limiting dilution and
480 monoclonal cell lines expressing eYFP-CEP90 were manually selected based on fluorescence.

481 RPE1 cells stably expressing HA-CEP83 under the control of tetracycline-inducible promoter were
482 a gift from Barbara Tanos and Bryan Tsou (Tanos et al., 2013). CEP83 expression was induced
483 with 1 µg/ml doxycycline (Fischer Chemical; Catalog BP26535) for 48 h.

484 *Cep90*$^{-/-}$ and *Mnr*$^{-/-}$ MEFs were derived from E8.5 embryos along with littermate WT control MEFs.
485 Cells were cultured in DMEM supplemented with 10% FBS (Invitrogen) and Glutamax-I
486 (Invitrogen), and subsequently immortalized by transduction with SV40 large T antigen.

487 All cell lines were routinely tested for mycoplasma contamination and found negative.

488 **Generation of *CEP90*$^{-/-}$, *MNR*$^{-/-}$ and *PCM1*$^{-/-}$ RPE1 cells by CRISPR/Cas9 gene targeting**

489 RNA guided targeting of *CEP90* and *MNR* was achieved by coexpression of Cas9 along with
490 guide RNAs. The pSpCas9 (BB)-2A-GFP (PX458) was a gift from Feng Zhang (Addgene plasmid
491 #48138; http://n2t.net/addgene:48138; RRID:Addgene_48138). The gRNA sequences used for
492 CEP90 and MNR were 5′-GATGAGGAAATATCATCCGT-3′ and 5′-
493 GTATAAAATACCCGACCACA-3′ respectively.

494 *PCM1*$^{-/-}$ RPE1 cells were generated by electroporating recombinant Cas9 along with sgRNAs
495 (CRISPRevolution sgRNA EZ kit, Synthego). The sgRNA targeting exon 4 of human *PCM1*: 5′-
496 GAAAAGAAUAAGAAAAAGUU-3′ was used. 1.5 nmol sgRNA was resuspended in 15 µl
497 nuclease-free TE for a final concentration of 100 µM (100 pmol/µl). The RNP mixture containing
498 1.8 µl of sgRNA with 3 µl (90 pmol) Truecut Cas9 v2 (Thermo Fisher; catalog A36498) in a total
499 volume of 5 µl was incubated at room temperature for 15 minutes. The RNP mixture was
500 electroporated into hTERT-RPE1 cells using the Neon transfection system (Thermo Fisher)

501 according to manufacturer's instruction using the following parameters: 1350 V pulse voltage, 20
502 ms pulse width and 2 pulses. All electroporated cells were serially diluted, and single colonies
503 screened by western blotting, immunofluorescence and PCR analyses. For genotyping, the
504 following PCR primers were used: 5′-TGGGATGCACTAAATTGCCTA-3′ and 5′-
505 TTACCTGCCGTTTGAAGACA-3′ for *CEP90* alleles, 5′- TCCAGTGAACCAACTCACAGA-3′ and
506 5′-TAGGAGCGTGGCTGTGTCTAT -3′ for MNR alleles, and 5′- ACAGGCCATGTTAATTTTTGCT
507 -3′ and 5′- CCATCCCCAGTGATTAAAATTC -3′ for *PCM1* alleles. PCR products were cloned and
508 sequenced.

509 **Plasmids and transfections**

510 Myc-DDK tagged *Mnr* (*4933427D14Rik*) cDNA in cloned in a pCMV6 plasmid was obtained from
511 Origene (MR211309). hTERT-RPE1 cells were transfected using TransIT-LT1 transfection
512 reagent (Mirus Bio) according to manufacturer guidelines.

513 For co-immunoprecipitation experiments in Fig. 5, C-terminal GFP-2x Strep-tagged full length and
514 truncation versions of CEP90 were cloned into pLVX-EF1α-IRES-Puro backbone and transfected
515 into 293T cells using TransIT-293 transfection reagent (Mirus Bio) according to manufacturer
516 guidelines.

517 **Antibodies**

518 The list of primary antibodies and the dilution they were used at are listed in Supplementary Table
519 1. Secondary antibodies conjugated to Alexa Fluor 488, 568 and 647 were purchased from
520 Thermo Fisher Scientific, and used at a 1:500 dilution.

521 **Immunofluorescence**

522 For immunostaining, cells were fixed with either 100% cold methanol for 3 minutes or 4%
523 paraformaldehyde in dPBS for 15 minutes at room temperature, and then incubated in blocking
524 buffer (2.5% BSA, 0.1% Triton-X 100 in PBS) for 1 hour at room temperature. Paraformaldehyde
525 fixed cells were permeabilized with 0.1% Triton X-100 in PBS for 15 minutes at room temperature
526 prior to addition of blocking buffer. Coverslips were incubated with primary antibodies in blocking
527 buffer overnight at 4 °C, washed three times with PBS and incubated in secondary antibodies in
528 blocking buffer for 1-2 h at room temperature. Nuclei were counterstained with Hoechst 33352
529 (Thermo Fisher Scientific; catalog H3570). Coverslips were washed three times with PBS and
530 mounted with Prolong Diamond (Thermo Fisher Scientific; catalog P36961).

531 In experiments requiring disruption of the microtubule cytoskeleton, cells were treated with 20 μM
532 Nocodazole (Sigma Aldrich; catalog SML1665) for 2 h at 37 ºC prior to fixation.

533 Identification of cell cycle stages was performed as described previously (Viol et al., 2020), using
534 the Click-iT EdU Alexa Fluor 555 imaging kit (Life Technologies). Briefly, *PCM1*$^{-/-}$ RPE1 cells were
535 treated with 10 μM EdU for 30 minutes and fixed in 100% cold methanol for 3 minutes. The Click-
536 IT reaction was performed according to manufacturer guidelines, and samples subsequently
537 processed for indirect immunofluorescence. Cells lacking CENPF and EdU in the nucleus were
538 categorized as G1. EdU-positive, CENPF-negative cells were categorized as S, while cells with
539 nuclear CENPF staining, without EdU staining were classified as being in G2.

540 **Super-resolution microscopy**

541 3D-SIM and 2D-SIM was performed using the DeltaVision OMX-SR microscope (GE Healthcare)
542 using the 60x/1.42 NA oil immersion PSF objective and three sCMOS cameras. Immersion oil
543 with refractive index of 1.518 was used for most experiments. Z stacks of 5-6 μm were collected
544 using a 0.125 μm step size. Raw images were reconstructed using SoftWorx 6.5.2 (GE
545 Healthcare) using default parameters.

546 Label-retention expansion microscopy was performed as described previously (Shi et al., 2019).
547 Briefly, RPE1 cells were cultured on 16-well chambered slides (Sigma; catalog GBL112358-8EA)
548 coated with 0.1% gelatin (Sigma Aldrich; catalog G1393). Cells were serum starved in Opti-MEM
549 to induce ciliation for 24 h prior to fixation. After incubation with primary antibodies, cells were
550 incubated with appropriate secondary antibodies conjugated to NHS-MA-biotin or NHS-MA-DIG.
551 After gel polymerization and proteinase K digestion, gels were stained with fluorescently labeled
552 streptavidin or digitonin antibodies and images were acquired on the DeltaVision OMX-SR.

553 **Fluorescence intensity measurements and statistical analyses**

554 For fluorescence intensity measurements, z stacks were acquired on the DeltaVision OMX-SR
555 using widefield settings. Identical laser power and exposure settings were used for control and
556 experimental samples. Average intensity projections were generated using Image J (Schneider
557 et al., 2012), and images transferred to CellProfiler image analysis software (McQuin et al., 2018).
558 Cilia number were quantified by using Hoechst stained nuclei to count the total number of cells,
559 and a cilia marker (ARL13B/Tubulin^{Ac}) to identify cilia using the object identification module in
560 CellProfiler using difference in signal intensity and size to segment cilia. For quantification of
561 centrosomal intensity, a mask around the centrosomal area was generated using a centrosomal
562 marker (γ-tubulin/FOP) to identify the centrosome in CellProfiler. This centrosomal mask was

563 used to determine fluorescence intensity (integrated intensity) and area (in pixels) for the channel
564 of interest. Fluorescence intensity values in a pericentrosomal area were used to measure
565 background. Cells were serum starved for 24 h prior to fixing, to synchronize cells in G0/G1 and
566 eliminate cell cycle-dependent alterations in centrosomal proteins. Data were exported to
567 Microsoft Excel, and graphs generated in GraphPad Prism 8.

568 Statistical analyses were performed using GraphPad Prism 8. Results represented are mean ±
569 standard deviation. Statistical differences between data sets were analyzed using one-way Anova
570 with Tukey's multiple comparison tests or a two-tailed unpaired student's t test. Data distribution
571 was assumed to be normal but this was not formally tested. P value < 0.05 was considered
572 significant and indicated with an asterisk. NS denotes not significant.

573 **Transmission electron microscopy**

574 For electron microscopy, cells were plated on 8-well Permanox slides (Nunc; catalog177445),
575 gently washed in 0.1 M phosphate buffer (PB) and fixed in 3.5% EM-grade glutaraldehyde
576 (Electron Microscopy Sciences; catalog 16210) in 0.1M Phosphate buffer (PB) for 10 minutes at
577 37 ºC. Fixative was removed, replaced with fresh fixative, and samples incubated at 4 ºC for 1 h.
578 Slides were washed three times with 0.1 M PB and processed for TEM as described previously
579 (Singla et al., 2010).

580 **Co-immunoprecipitation and Western Blotting**

581 Cells grown in 10 cm petri dishes were washed twice with ice-cold dPBS and lysed for 30 minutes
582 on ice with frequent pipetting. Lysis buffer used was 10 mM Tris/Cl pH 7.5, 150 mM NaCl, 0.5 mM
583 EDTA, 0.5 % Nonidet P40 substitute supplemented with 1x protease inhibitor (Roche cOmplete
584 mini, EDTA free; catalog 4693159001) and 1x phosphatase inhibitor (Thermo Fisher PhosStop;
585 catalog 4906845001) cocktails. Lysates were cleared by centrifugation at 17,000 g for 10 minutes
586 at 4 ºC. GFP-trap magnetic agarose (Chromotek; catalog gtma-10) was used for eYFP-CEP90
587 co-immunoprecipitation assays, and HA-magnetic beads (Pierce; catalog 88837) for CEP83-HA
588 co-immunoprecipitation assays. Co-immunoprecipitation assays were performed according to
589 manufacturer guidelines. Samples were separated on 4-15% Criterion TGX Precast gels (Bio-
590 Rad), and transferred to Immobilon PVDF membranes (0.45 µm pore size) for
591 chemiluminescence detection.

592 **Mass spectrometry and data analysis**

593 Eluates obtained after co-immunoprecipitation were reduced by the addition of 1 mM DTT at 60°C
594 for 15 minutes, cooled to room temperature, alkylated by the addition of 3 mM iodoacetamide for

595 45 minutes in the dark. Alkylation was quenched by the addition of 3 mM DTT and proteins were
596 digested overnight at 37°C with 1 μg trypsin (0.5 μg/μl; Promega). Following digestion, peptides
597 were acidified with trifluoroacetic acid (0.5% final, pH < 2), desalted using UltraMicroSpin Columns
598 (PROTO 300 C18 300Å; The NEST Group) according to manufacturer's specifications, and dried
599 under vacuum centrifugation. Samples were resuspended in 4% formic acid, 4%
600 acetonitrile solution, and separated by a reversed-phase gradient over a nanoflow column (360
601 μm O.D. x 75 μm I.D.) packed with 25 cm of 1.8 μm Reprosil C18 particles with (Dr. Maisch). The
602 HPLC buffers were 0.1% formic acid and 100% acetonitrile on 0.1% formic acid for buffer A and
603 B respectively. The gradient was operated at 400 nL/min from 0 to 28% buffer B over 40min,
604 followed by a column wash at 95% B, with a total acquisition time of 50 min. Eluting peptides were
605 analyzed in on a Bruke timsTOF Pro mass spectrometry system equipped with a Bruker
606 nanoElute high-pressure liquid chromatography system interfaced via a captiveSpray source. A
607 data-dependent PASEF acquisition (Meier et al., 2018) method was used for data acquisition
608 using the following parameters: 100-1700 m/z range, 0.85-1.30 V*s/cm^2 trapped ion mobility
609 range, 1600V spray voltage, intensities of 200,000 were repeated for in PASEF 0 times, intensities
610 of 100,000 to 200,000 were repeated for in PASEF 5 times, intensities of less than 100,000 were
611 repeated for in PASEF 10 times, 4 PASEF MS/MS scans with a total cycle time of 0.53 s, and
612 active exclusion for 0.4 min. Data was search against the human proteome database (canonical
613 sequences downloaded from Uniprot 3/21/2018) using MaxQuant (Cox and Mann, 2008;
614 Prianichnikov et al., 2020). Peptide and protein identifications were filtered to 1% false-discovery
615 rate at the peptide and protein level, and protein-protein interaction analysis was performed using
616 SAINTexpress (Teo et al., 2014). The mass spectrometry data files (raw and search results) have
617 been deposited to the ProteomeXchange Consortium (Deutsch et al., 2017; Perez-Riverol et al.,
618 2019) (http://proteomecentral.proteomexchange.org) via the PRIDE partner repository with
619 dataset identifier PXD022372.

620 **Online supplemental material**

621 **Fig. S1** depicts CRISPR/Cas9-mediated mutations of *CEP90*, *MNR* and *PCM1* and effect on
622 corresponding proteins as assessed by immunoblotting. **Fig. S2** shows that overexpressed MNR
623 localizes to microtubules and sequesters endogenous OFD1. **Fig. S3** shows that CEP90 and
624 MNR regulate distal appendage assembly irrespective of whether the cell possesses a cilium.
625 **Fig. S4** includes serial-section TEMs of WT, *Cep90*$^{-/-}$ and *MNR*$^{-/-}$ cells. **Fig. S5** shows that CEP90
626 and MNR regulate distal appendage assembly independent of Talpid3 recruitment and removal
627 of daughter centriole proteins. **Table 1** lists all primary antibodies used in this study.

ACKNOWLEDGEMENTS

We thank E Yu for help with animal husbandry and genotyping of mice used in this study. We thank members of the Reiter and Yoder labs for helpful discussions. This work was supported by NIH R01HD089918 to J.F.R and B.Y., NIH R01R01DE029454 and R01AR054396 to J.F.R., the Valencian Council for Innovation, Universities, Science and Digital Society (PROMETEO/2019/075) to J.M.G-V and the Spanish Ministry of Science, Innovation and Universities (PCI2018-093062) to V.H-P, NIH NIGMS R01GM124334 to B.H., by the NIH Pathway to Independence Award K99GM126136/R00GM126136 and the UCSF Mary Anne Koda-Kimble Seed Award for Innovation to X.S. D.K. is supported a Jane Coffin Childs Postdoctoral Fellowship, and the Program for Breakthrough Biomedical Research Award, which is partially funded by the Sandler Foundation. B. H. and J.F.R. are Chan Zuckerberg Biohub Investigators.

The authors declare no competing financial interests.

Author contributions: Conceptualization: D. Kumar, B. Yoder and J.F Reiter; data acquisition: D. Kumar, A. Rains, V. Herranz-Perez, Q. Lu, X. Shi, D.L. Swaney, E. Stevenson; funding acquisition: D. Kumar, N. J. Krogan, C. Westlake, J. M. Garcia-Verdugo, B. Huang, B. Yoder and J.F. Reiter; writing - original draft: D. Kumar; writing - review and editing: D. Kumar, A. Rains, V. Herranz-Perez, B. Yoder, J.F. Reiter.

FIGURE LEGENDS

Figure 1. CEP90 localizes to centriolar satellites and the distal centriole. a. 3D-SIM of immunostained RPE1 cells reveals localization of CEP90 (yellow) at centriolar satellites (PCM1, cyan) and centrioles (Tubulin^{Ac}, magenta) in wild type, cycling RPE1 cells. Scale bar = 1 µm. **b**. Treatment of serum-starved RPE1 cells with nocodazole disperses the centriolar satellites, highlighting 3D-SIM of CEP90 (yellow) rings at centrioles (γ-tubulin, magenta). Distal appendage component CEP164 (cyan) indicates the mother centriole in C and D. Scale bar = 1 µm. **c**. 3D-SIM of serum-starved *PCM1*$^{-/-}$ RPE1 cells shows that CEP90 (yellow) localizes to centrioles (γ-tubulin, magenta) independent of centriolar satellites. Scale bar of main panel and insets = 1 µm and 0.5 µm respectively. **d**. 3D-SIM confirms localization of CEP90 (yellow) at centrioles (γ-tubulin, magenta) in nocodazole-treated, serum-starved eYFP-CEP90 expressing *PCM1*$^{-/-}$ RPE1 cells. Scale bar = 1 µm. **e**. Quantification of eYFP-CEP90, Centrobin and CEP164 fluorescence intensity at daughter (DC) and mother (MC) centrioles from n = 10-20 cells. Horizontal lines indicate means ± SEM. Asterisks indicate $p<0.05$ determined using unpaired t test and ns = not significant. **f**. LR-ExSIM of RPE1 cells immunostained for CEP90 (yellow) and CEP164

660 (magenta) reveals that rings of CEP90 are comprised of discrete puncta. CEP90 rings are smaller
661 and more proximal to CEP164 rings. Scale bar = 1 μm. **g**. Example of an LR-ExSIM image of a
662 radially oriented centriole used to quantify the number and angle between adjacent puncta of
663 CEP90. Scale bar = 0.5 μm. **h**. Histogram of number of discrete puncta of CEP90 and CEP164
664 observed per centriole in LR-ExSIM images. n = 12-17 measurements. **i**. Histogram of the angular
665 spacing between adjoining centriolar CEP90 puncta observed by LR-ExSIM. n = 66
666 measurements. **j**. Schematic of the ring of CEP90 punctae (yellow), distal appendages (magenta),
667 and sub-distal appendages (blue) at the distal centriole. CEP90 decorates the distal end of mother
668 and daughter centrioles.

669 **Figure 2. CEP90 forms a complex with OFD1 and MNR. a.** Schematic depicting workflow used
670 to identify CEP90 interactors at centriolar satellites and centrioles using WT and *PCM1*$^{-/-}$ RPE1
671 cells. *PCM1*$^{-/-}$ cells localize CEP90 to the distal centriole and WT cells localize CEP90 to the distal
672 centriole and centriolar satellites. **b**. Venn diagram comparing high confidence interactors of
673 CEP90 in WT and *PCM1*$^{-/-}$ RPE1 cells. **c**. Interactome dot representation of selected CEP90
674 interactors identified in the proteomic screen. Hits were grouped based on their cellular
675 localization. Average number of peptide spectra is represented by dot shade. Abundance of a
676 peptide spectrum produced in relation to the most abundant spectrum is depicted by dot size.
677 Bayesian false discovery rate (BFDR) is represented by rim color. **d**. Immunoblot of a subset of
678 CEP90 interactions identified by proteomics were validated by co-immunoprecipitation (IP).
679 CEP90 interacts with PCM1, OFD1 and MNR, but not α-tubulin or GAPDH. FT, flow through.
680 Specific MNR band is indicated with an asterisk. The top band is nonspecific as it is undiminished
681 in the MNR knockout cell lysates. **e.** Coulson plot showing the phylogenetic distribution of a subset
682 of centriolar proteins in select ciliated metazoan species. Orthologs identified with high confidence
683 are indicated with a filled circle, and a subset of CEP90 interactors further explored in this study
684 are highlighted in blue. The dendrogram on top (made using iTOL (Ciccarelli et al., 2006)) shows
685 the evolutionary relationship between species.

686 **Figure 3. CEP90 co-localizes with OFD1 and MNR. a.** Immunostaining of RPE1 cells for CEP90
687 (yellow), MNR (cyan) and γ-tubulin (magenta) demonstrating that CEP90 co-localizes with MNR
688 at centriolar satellites. Scale bar = 2 μm. **b.** 3D-SIM of RPE1 cells treated with nocodazole to
689 disperse centriolar satellites highlights co-localization of CEP90 (yellow) and MNR (cyan) at
690 centrioles (γ-tubulin, magenta). Scale bar = 1 μm. **c**. Immunostaining of OFD1 (yellow), MNR
691 (cyan) and γ-tubulin (magenta) reveals CEP90 and MNR co-localization at centriolar satellites.
692 Scale bar = 2 μm. **d**. 3D-SIM of immunostained cells treated with nocodazole reveals a ring of

693 OFD1 (yellow) co-localizing with MNR (cyan) at centrioles (γ-tubulin, magenta). Scale bar =1 μm.
694 **e**. Measurements of ring diameters measured in 3D-SIM images. For distal centriole proteins, ring
695 diameters were measured at the mother (MC) and daughter centriole (DC). Scatter dot plot shows
696 mean ± SD. Asterisks indicate $p < 0.05$, and ns indicate not significant determined using unpaired
697 t test. n = 13-22 centrioles. **f**. Schematic representation of a radial view of a mother centriole with
698 distal appendages (purple), OFD1 (orange), CEP90 (yellow) and MNR (green). **g**. Localization of
699 distal centriole proteins (yellow) to centrioles (γ-tubulin, magenta) is cell cycle dependent. Cells
700 in G1 were identified as lacking both EdU and CENPF staining, cells in S as being positive for
701 EdU but lacking CENPF, and cells in G2 as being positive for CENPF but lacking EdU staining.
702 Two puncta of CEP90, OFD1 and MNR localized were observed at one centrosome during G1
703 and S, and four puncta at two centrosomes after centrosome duplication during G2. Scale bar of
704 main panel and insets = 5 μm and 0.5 μm respectively.

705 **Figure 4. CEP90 and MNR are essential for ciliogenesis. a**. WT, *CEP90*$^{-/-}$ and *MNR*$^{-/-}$ serum
706 starved RPE1 cells were immunostained for cilia (ARL13B, magenta), centrosomes (γ-tubulin,
707 yellow) and nuclei (Hoechst, blue). Scale bar = 10 μm. **b**. Quantification of ciliation frequency of
708 WT, *CEP90*$^{-/-}$ and *MNR*$^{-/-}$ RPE1 cells serum starved for times indicated. n >100 cells from two
709 biological replicates. **c.** Images of control, *Cep90*$^{-/-}$ and *Mnr*$^{-/-}$ embryos at embryonic day (E) 9.5.
710 Arrows point to pericardial edema observed in mutant embryos. **d**. Whole-mount immunostaining
711 of nodes of littermate control and *Cep90*$^{-/-}$ embryos at E8.5 for centrosomes (γ-tubulin, yellow),
712 cilia (Tubulin^{Ac}, magenta) and nuclei (Hoechst, blue). Arrows in control image point to cilia
713 projecting into the node lumen, which are absent in *Cep90*$^{-/-}$ embryos. Scale bar of main panel
714 and insets = 5 μm and 2 μm respectively. **e**. *In situ* hybridization for *Gli1* in E8.5 littermate control
715 and *Cep90*$^{-/-}$ embryos, revealing decreased expression in the absence of CEP90 indicative of
716 disrupted Hedgehog signaling. Scale bar = 5 μm. **f**. Immunostaining of E9.5 neural tube sections
717 of littermate control and *Mnr*$^{-/-}$ embryos for centrosomes (FOP, yellow), cilia (ARL13B, magenta)
718 and nuclei (Hoechst, blue), indicating that MNR is required for ciliogenesis in vivo. Scale bar = 5
719 μm. **g**. MEFs derived from *Cep90*$^{+/+}$ and *Cep90*$^{-/-}$ embryos were serum starved for 24 h and
720 immunostained for cilia (ARL13B, magenta), centrosomes (γ-tubulin, yellow) and nuclei (Hoechst,
721 blue). Scale bar = 10 μm. **h**. Quantification of ciliation frequency shows loss of cilia in *Cep90*$^{-/-}$
722 MEFs. Bar graph shows mean ± SEM. Asterisks indicate $p < 0.05$ determined using unpaired t
723 test. n >100 cells from two biological replicates. **i**. qRT-PCR of HH target genes *Gli1* and *Ptch1*
724 in serum-starved *Cep90*$^{+/+}$ and *Cep90*$^{-/-}$ MEFs stimulated with 200nM SAG for 24h relative to
725 DMSO-treated controls. Bar graph shows mean ± SEM. Asterisks indicate $p < 0.05$ determined
726 using unpaired t test. n = 3 biological replicates. **j**. MEFs derived from *Mnr*$^{+/+}$ and *Mnr*$^{-/-}$ embryos

727 were serum starved for 24 h and immunostained for cilia (ARL13B, magenta), centrosomes (γ-
728 tubulin, yellow) and nuclei (Hoechst, blue). Scale bar = 10 μm. **k**. Quantification of ciliation
729 frequency shows loss of cilia in *Mnr*$^{-/-}$ MEFs. Bar graph shows mean ± SEM. Asterisks indicate p
730 <0.05 determined using unpaired t test. n >100 cells from two biological replicates. **l**. qRT-PCR
731 of HH target genes *Gli1* and *Ptch1* in serum-starved *Mnr*$^{+/+}$ and *Mnr*$^{-/-}$ MEFs stimulated with 200nM
732 SAG for 24h relative to DMSO-treated controls. Bar graph shows mean ± SEM. Asterisks indicate
733 p <0.05 determined using unpaired t test. n = 3 biological replicates.

734 **Figure 5. *CEP90* ciliopathy mutations affect ciliogenesis and centriolar satellite**
735 **morphology. a**. Schematic representation of full length (FL) human CEP90, truncation constructs
736 and disease-associated mutations. Coiled-coil (CC) domains identified by MARCOIL
737 (Zimmermann et al., 2018) at 90% threshold are indicated in cyan. **b**. Quantification of ciliation
738 frequency of *CEP90*$^{-/-}$ RPE1 (control), and *CEP90*$^{-/-}$ cells expressing mNeonGreen (mNG) tagged
739 disease-variants and truncations of CEP90. Graph shows mean ± SEM, and asterisks indicate p
740 <0.05 determined by one-way ANOVA. n >100 cells from two biological replicates. **c**. *CEP90*$^{-/-}$
741 RPE1 cells, and *CEP90*$^{-/-}$ cells expressing the denoted mNG-tagged versions of CEP90 were
742 serum starved for 24 h and immunostained for cilia (ARL13B), centriolar satellites (CEP131) and
743 mNeonGreen. Scale bar = 2 μm. **d**. Immunoprecipitation of GFP-tagged FL and truncation
744 constructs of CEP90 blotted for GFP and OFD1. **e**. Quantification of OFD1 band intensities
745 relative to corresponding GFP input band intensities. **f**. Immunoprecipitation of GFP-tagged FL
746 and truncation constructs of CEP90 blotted for GFP and MNR. **g**. Quantification of MNR band
747 intensities relative to corresponding GFP input band intensities. Asterisk represents MNR band,
748 top band is non-specific.

749 **Figure 6. MNR, but not CEP90, restricts centriole length. a.** 3D-SIM images of WT, *CEP90*$^{-/-}$
750 and *MNR*$^{-/-}$ RPE1 cells immunostained for cilia/centrioles (Tubulin^{Ac}, magenta) and CEP162
751 (yellow), a distal centriolar protein. Scale bar of main panel and insets = 1 μm and 0.5 μm
752 respectively.**b**. Graph of centriolar lengths measured using 3D-SIM images. Centriole lengths are
753 longer and have a wider distribution in *MNR*$^{-/-}$ cells than in WT or *CEP90*$^{-/-}$ cells. Lines indicate
754 mean ± SEM. Asterisks indicate p <0.05 determined using one-way ANOVA. n = 14-30 centrioles.
755 **c**. Histogram of centriole lengths observed in WT, *MNR*$^{-/-}$ and *CEP90*$^{-/-}$ cells. n = 14-30 centrioles.
756 **d**. Serial section TEM confirms the presence of elongated centrioles in *MNR*$^{-/-}$ RPE1 cells. Scale
757 bar = 500 nm. **e.** Centriole lengths of WT and *MNR*$^{-/-}$ RPE1 cells measured using TEM images.
758 Horizontal lines indicate means ± SEM, and asterisks indicate p<0.05 determined using unpaired
759 t test. n = 8 centrioles per condition. **f**. WT and *MNR*$^{-/-}$ RPE1 cells were serum-starved and

760 immunostained with antibodies to Tubulin^{Ac} and sub-distal appendage component Ninein to
761 distinguish mother (MC) and daughter centrioles (DC). Graph of centriolar lengths measured
762 using 3D-SIM. MNR restrains centriole lengthening of both mother and daughter centrioles. Lines
763 indicate mean ± SEM. Asterisks indicate p <0.05 determined using unpaired t-test. n = 10-35
764 measurements. **g**. Schematic depicting distinct roles of CEP90 and MNR in regulating centriole
765 length. **h**. 3D-SIM imaging of serum-starved WT, *CEP90*$^{-/-}$ and *MNR*$^{-/-}$ RPE1 cells immunostained
766 for OFD1 (yellow), centrioles (γ-tubulin, cyan) and cilia (Tubulin^{Ac}, magenta). Boxed regions are
767 depicted in insets throughout. OFD1 localizes to centrioles in WT and *CEP90*$^{-/-}$, but not *MNR*$^{-/-}$
768 cells. Scale bar = 1 μm. **i**. Quantification of OFD1 fluorescence intensity at centrioles in WT,
769 *CEP90*$^{-/-}$ and *MNR*$^{-/-}$ cells. Horizontal lines indicate means ± SEM. Asterisks indicate p<0.05
770 determined using one-way ANOVA. n = 64-187 cells.

771 **Figure 7. CEP90 and MNR are required for early ciliogenesis. a** WT, *CEP90*$^{-/-}$ and *MNR*$^{-/-}$
772 RPE1 cells immunostained for IFT88 (yellow), centrioles (γ-tubulin, cyan) and cilia (Tubulin^{Ac},
773 magenta. IFT88 is not recruited to the centrosome of *CEP90*$^{-/-}$ or *MNR*$^{-/-}$ cells. **b.** Quantification of
774 IFT88 fluorescence intensity at WT, *CEP90*$^{-/-}$ and *MNR*$^{-/-}$ centrosomes. Lines indicate mean ±
775 SEM. Asterisks indicate p <0.05 determined using unpaired t test. n = 38-63 measurements. **c**.
776 WT, *CEP90*$^{-/-}$ and *MNR*$^{-/-}$ serum-starved RPE1 cells immunostained for CP110 (yellow), centrioles
777 (γ-tubulin, cyan) and cilia (Tubulin^{Ac}, magenta). Scale bar = 1 μm. **d**. Quantification of whether
778 CP110 localizes to one or two centrioles. In the absence of CEP90 or MNR, CP110 continues to
779 localize to the distal mother centriole. n>50 cells from 2 independent experiments. Scale bar = 1
780 μm. **e**. WT, *CEP90*$^{-/-}$ and *MNR*$^{-/-}$ serum-starved RPE1 cells immunostained for CEP97 (yellow),
781 γ-tubulin (cyan) and Tubulin^{Ac} (magenta). Scale bar = 1 μm. **f**. Quantification of whether CEP97
782 localizes to one or two centrioles. As with CP110, CEP90 and MNR are required to remove CEP97
783 from the distal mother centriole. n>50 cells from 2 independent experiments. Scale bar = 1 μm.
784 **g**. 3D-SIM images of RPE1 cells immunostained for Myo-Va (yellow) and centrioles (γ-tubulin,
785 magenta). Myo-Va can not localize near centrosomes (left), can localize to preciliary vesicles
786 (denoted centrosomal Myo-Va, middle), or can localize to the ciliary pocket (denoted ciliary Myo-
787 Va, right). Scale bar = 1 μm. **h**. Quantification of three distinct Myo-Va staining patterns in WT,
788 *CEP90*$^{-/-}$ and *MNR*$^{-/-}$ cells. n>50 cells from 2 independent experiments. **i.** Serial section TEM
789 images of serum-starved *Cep90*$^{+/+}$ and *Cep90*$^{-/-}$ MEFs confirms the absence of preciliary vesicle
790 docking at the *Cep90*$^{-/-}$ mother centriole. Scale bar = 200 nm. n= 9 cells for both genotypes. **j.**
791 Serial-section TEM images of WT and *MNR*$^{-/-}$ RPE1 cells confirms the absence of preciliary
792 vesicle vesicle docking at the *MNR*$^{-/-}$ mother centriole. Scale bar = 250 nm. n= 10 cells for WT

793 and n= 6 for *MNR*$^{-/-}$ cells. **k**. Model based on our data highlighting the role of CEP90 and MNR in
794 maturation of the mother centriole.

795 **Figure 8. CEP90 and MNR recruit distal appendage components to the mother centriole.**
796 3D-SIM images and quantification of centrosomal intensity of WT, *CEP90*$^{-/-}$ and *MNR*$^{-/-}$ RPE1 cells
797 immunostained for γ-tubulin (cyan), Tubulin^{Ac} (magenta) and distal centriole components (yellow)
798 CEP83 (**a,b**), FBF1 (**c,d**), SCLT1 (**e,f**), ANKRD26 (**g,h**) and CEP164 (**i,j**). Scale bar = 1 μm.
799 Horizontal lines in scatter dot plots indicate means ± SEM. Asterisks indicate p<0.001 determined
800 by one-way ANOVA. n ≥ 40 measurements per condition.

801 **Figure 9. Centriolar satellites are dispensable for distal appendage assembly at the mother**
802 **centriole. a.** 3D-SIM images of WT, *CEP90*$^{-/-}$ and *MNR*$^{-/-}$ RPE1 cells immunostained with
803 antibodies to PCM1, a centriolar satellite marker, ARL13B and γ-tubulin. Scale bar = 2 μm. **b**.
804 Quantification of PCM1 intensity in the pericentrosomal area. PCM1-positive centriolar satellites
805 fail to accumulate around centrosomes in *CEP90*$^{-/-}$, but not in *MNR*$^{-/-}$ cells. Lines indicate mean ±
806 SEM. Asterisks indicate p <0.05 determined using ordinary one-way ANOVA. n = 37-44
807 measurements. **c**. Ciliogenesis is disrupted in *PCM1*$^{-/-}$ RPE1 cells at 24 h post serum starvation.
808 n >100 cells from two biological replicates. **d**. WT and *PCM1*$^{-/-}$ RPE1 cells were serum starved
809 for 24 h and stained with antibodies to CEP83, γ-tubulin (centrosome marker) and Tubulin^{Ac} (cilia
810 marker). 3D-SIM imaging reveals ring of CEP83 at the mother centrioles in *PCM1*$^{-/-}$ RPE1 cells.
811 Scale bar = 1 μm. **e**. Quantification of CEP83 fluorescence intensity at centrioles. Scatter dot plots
812 show mean ± SEM. NS = not significant, determined using unpaired t test. n = 53-124
813 measurements. **f**. WT and *PCM1*$^{-/-}$ RPE1 cells were serum starved for 24 h and stained with
814 antibodies to SCLT1, γ-tubulin (centrosome marker) and ARL13B (cilia marker). 3D-SIM imaging
815 reveals ring of SCLT1 at the mother centrioles in WT and *PCM1*$^{-/-}$ RPE1 cells. Scale bar = 1 μm.
816 **g**. Quantification of SCLT1 fluorescence intensity at centrioles. Scatter dot plots show mean ±
817 SEM. NS = not significant, determined using unpaired t test. n = 26-28 measurements. **h**. WT and
818 *PCM1*$^{-/-}$ RPE1 cells were serum starved for 24 h and stained with antibodies to CEP164 and γ-
819 tubulin (centrosome marker). 3D-SIM imaging reveals ring of CEP164 at the mother centrioles in
820 *PCM1*$^{-/-}$ RPE1 cells. Scale bar = 1 μm. **i**. Quantification of CEP164 fluorescence intensity at
821 centrioles. Scatter dot plots show mean ± SEM. Asterisks indicate p< 0.001, determined using
822 unpaired t test. n = 40-60 measurements. **j**. Representative TEM images of WT and *PCM1*$^{-/-}$ RPE1
823 cells serum starved for 1 hour. Distal appendages are marked with red arrows.

824

825 **Figure 10. MNR recruits CEP90 which recruits CEP83 to build distal appendages. a.** 3D-SIM
826 imaging of WT, *CEP90*$^{-/-}$ and *MNR*$^{-/-}$ serum-starved RPE1 cells immunostained for CEP90
827 (yellow), γ-tubulin (cyan) and Tubulin^{Ac} (magenta). Scale bar = 1 μm. **b**. Quantification of CEP90
828 fluorescence intensity at centrioles. Horizontal lines in scatter dot plots indicate means ± SEM.
829 Asterisks indicate $p < 0.0001$, ns = not significant, determined using one-way ANOVA. n = 31-37
830 measurements. CEP90 fails to localize to *MNR*$^{-/-}$ and *CEP90*$^{-/-}$ centrioles, although protein levels
831 of CEP90 remained unchanged in *MNR*$^{-/-}$ RPE1 cells (Supplementary Fig. 1d). **c**. 3D-SIM imaging
832 of WT, *CEP90*$^{-/-}$ and *MNR*$^{-/-}$ serum-starved RPE1 cells immunostained for MNR (yellow), γ-tubulin
833 (cyan) and CEP164 (magenta). Scale bar = 1 μm. **d.** Quantification of MNR fluorescence intensity
834 at centrioles. Horizontal lines in scatter dot plots indicate means ± SEM. Asterisks indicate $p <$
835 0.0001, determined using one-way ANOVA. n = 73-122 measurements. MNR localization is
836 reduced but present at *CEP90*$^{-/-}$ centrioles. **e**. Quantification of Talpid3 diameter at mother (MC)
837 and daughter centrioles (DC) in serum-starved WT and *CEP90*$^{-/-}$ cells. Horizontal lines in scatter
838 dot plots indicate means ± SEM. Asterisks indicate $p < 0.05$ determined using one-way ANOVA,
839 ns = not significant. n = 11-16 measurements. The Talpid3 ring diameter is increased at WT
840 mother centrioles, but not at *CEP90*$^{-/-}$ mother centrioles. **f**. Quantification of OFD1 diameter at
841 mother (MC) and daughter centrioles (DC) in serum-starved WT and *CEP90*$^{-/-}$ cells. Horizontal
842 lines in scatter dot plots indicate means ± SEM. Asterisks indicate $p < 0.05$, determined using
843 one-way ANOVA. n = 17-20 measurements. In the absence of CEP90, the mother centriole ring
844 of OFD1 does not expand as in wild-type cells. **g**. WT or RPE1 cells expressing CEP83-HA were
845 lysed, immunoprecipitated with anti-HA antibody bound beads and immunoblotted with antibodies
846 to HA and CEP90. **h**. Model of the hierarchical recruitment of the DISCO complex. MNR
847 recruitment of OFD1 restrains centriole elongation and MNR recruits CEP90 which, in turn,
848 recruits CEP83, the base of the distal appendage.

849

850 **SUPPLEMENTARY FIGURES:**

851 **SUPPLEMENTARY FIGURE 1. Generation of *CEP90*$^{-/-}$, *MNR*$^{-/-}$ and *PCM1*$^{-/-}$ cell lines.**
852 Sequence analysis of genomic DNA isolated from control and *CEP90*$^{-/-}$ (**a**), *MNR*$^{-/-}$ (**b**) and *PCM1*$^{-}$
853 $^{/-}$ (**c**) RPE1 cell lines generated using CRISPR-Cas9. Insertions and deletions, and translation
854 products resulting from genome editing are indicated. **d**. Immunoblot analysis of whole cell lysates
855 from control, *CEP90*$^{-/-}$, *MNR*$^{-/-}$ and *PCM1*$^{-/-}$ RPE1 cell lines confirms loss of protein in mutant cell
856 lines. Specific MNR band is indicated with an asterisk, top band is non-specific.

857 **SUPPLEMENTARY FIGURE 2. Overexpressed MNR localizes to microtubules and recruits**
858 **endogenous OFD1. a.** RPE1 cells transiently transfected with myc-tagged MNR and
859 immunostained with antibodies to myc-tag and α-tubulin. Scale bar = 10 μm. **b.** RPE1 cells
860 transiently transfected with myc-tagged MNR, and immunostained with antibodies to myc-tag and
861 OFD1. Scale bar = 10 μm. **c**. RPE1 cells transiently transfected with myc-tagged MNR, and
862 immunostained with antibodies to myc-tag and CEP90. Scale bar = 10 μm. **d**. RPE1 cells
863 transiently transfected with myc-tagged MNR, and immunostained with antibodies to myc-tag and
864 FOPNL. Scale bar = 10 μm.

865 **SUPPLEMENTARY FIGURE 3. CEP90 and MNR regulate distal appendage assembly**
866 **irrespective of ciliation status. a**. Cycling WT, *CEP90*$^{-/-}$ and *MNR*$^{-/-}$ RPE1 cells stained with
867 antibodies to IFT88, γ-tubulin (centrosome marker) and Tubulin^{Ac} (cilia and centriole marker). 3D-
868 SIM imaging reveals IFT88 at the centrosome in WT cells, but not in *CEP90*$^{-/-}$ and *MNR*$^{-/-}$ cells.
869 Scale bar for main panel and insets = 1 μm. **b**. Quantification of IFT88 fluorescence intensity at
870 centrioles. Scatter dot plots show mean ± SEM. Asterisks indicate $p<0.001$, determined using
871 one-way ANOVA. n = 73-96 measurements. **c**. Cycling WT, *CEP90*$^{-/-}$ and *MNR*$^{-/-}$ RPE1 cells
872 immunostained for CP110 (yellow), centrioles (FOP, cyan) and Tubulin^{Ac} (cilia and centriole
873 marker, magenta). Scale bar = 1 μm. **d**. Quantification of CP110 foci. **e**. Cycling WT, *CEP90*$^{-/-}$ and
874 *MNR*$^{-/-}$ RPE1 cells stained with antibodies to FBF1, γ-tubulin (centrosome marker) and Tubulin^{Ac}
875 (cilia and centriole marker). 3D-SIM imaging reveals FBF1 at the mother centriole in WT cells, but
876 not in *CEP90*$^{-/-}$ and *MNR*$^{-/-}$ cells. Scale bar for main panel and insets = 1 μm. **f**. Quantification of
877 FBF1 fluorescence intensity at centrioles. Scatter dot plots show mean ± SEM. Asterisks indicate
878 $p<0.001$, determined using one-way ANOVA. n = 21-45 measurements. **g**. Cycling WT, *CEP90*$^{-/-}$
879 and *MNR*$^{-/-}$ RPE1 cells stained with antibodies to CEP164, γ-tubulin (centrosome marker) and
880 Tubulin^{Ac} (cilia and centriole marker). 3D-SIM imaging reveals CEP164 at one of the two
881 centrioles in WT cells, but not in *CEP90*$^{-/-}$ and *MNR*$^{-/-}$ cells. Scale bar for main panel and insets =
882 1 μm. **h**. Quantification of CEP164 fluorescence intensity at centrioles. Scatter dot plots show
883 mean ± SEM. Asterisks indicate $p<0.001$, determined using one-way ANOVA. n = 37-53
884 measurements.

885 **SUPPLEMENTARY FIGURE 4. Serial section TEM confirms loss of distal appendages in**
886 **cells lacking CEP90 or MNR. a.** TEM images of*Cep90*$^{+/+}$ and *Cep90*$^{-/-}$ MEF cells confirms the
887 absence of preciliary vesicle vesicle docking, and distal appendages at the *Cep90*$^{-/-}$ mother
888 centriole. Scale bar = 500 nm. Blue arrowheads indicate subdistal appendages, and pink
889 arrowheads indicate distal appendages. CP indicate ciliary pocket. **b.** TEM images of WT and

890 *MNR*$^{-/-}$ RPE1 cells confirms the absence of preciliary vesicle docking and distal appendages at
891 the *MNR*$^{-/-}$ mother centriole. Centrioles are hyper-elongated in the absence of MNR. Scale bar =
892 500 nm. Blue arrowheads indicate subdistal appendages, and pink arrowheads indicate distal
893 appendages. CP indicate ciliary pocket.

894 **SUPPLEMENTARY FIGURE 5. CEP90 regulates distal appendage assembly independent**
895 **of Talpid3 recruitment and removal of Centrobin. a.** 3D-SIM imaging of serum-starved WT,
896 *CEP90*$^{-/-}$ and *MNR*$^{-/-}$ RPE1 cells immunostained for Ninein (yellow), centrioles (γ-tubulin, cyan)
897 and cilia (ARL13B, magenta). Boxed regions are depicted in insets throughout. Ninein localizes
898 to centrioles in WT, *CEP90*$^{-/-}$ and *MNR*$^{-/-}$ cells. Scale bar = 1 μm. **b**. Quantification of Ninein
899 fluorescence intensity at centrioles in WT, *CEP90*$^{-/-}$ and *MNR*$^{-/-}$ cells. Horizontal lines indicate
900 means ± SEM. Asterisks indicate $p<0.05$ determined using one-way ANOVA, ns indicates not
901 significant. n = 36-45 measurements. **c**. 3D-SIM imaging of serum-starved WT, *CEP90*$^{-/-}$ and
902 *MNR*$^{-/-}$ RPE1 cells immunostained for CEP170 (yellow), centrioles (γ-tubulin, cyan) and cilia
903 (Tubulin^{Ac}, magenta). Boxed regions are depicted in insets throughout. CEP170 localizes to
904 centrioles in WT, *CEP90*$^{-/-}$ and *MNR*$^{-/-}$ cells. Scale bar = 1 μm. **d**. Quantification of CEP170
905 fluorescence intensity at centrioles in WT, *CEP90*$^{-/-}$ and *MNR*$^{-/-}$ cells. Horizontal lines indicate
906 means ± SEM. Asterisks indicate $p<0.05$ determined using one-way ANOVA. n = 73-99
907 measurements. **e.** Immunoblot of distal appendage proteins CEP83 and CEP164 in WT, *CEP90*$^{-}$
908 $^{/-}$, *MNR*$^{-/-}$ and *PCM1*$^{-/-}$ RPE1 cells. **f**. Co-immunoprecipitation of daughter centriole proteins
909 Centrobin and CEP120 with CEP90. IP indicates eluate and FT indicates flow through **g**. WT,
910 *CEP90*$^{-/-}$ and *MNR*$^{-/-}$ RPE1 cells were serum starved for 24 h and stained with antibodies to
911 Talpid3, γ-tubulin (centrosome marker) and ARL13B (cilia marker). 3D-SIM imaging reveals ring
912 of Talpid3 at mother and daughter centrioles. Scale bar = 1 μm for main panels and insets. **h**.
913 Quantification of Talpid3 fluorescence intensity at centrioles. Scatter dot plots show mean ± SEM.
914 Asterisks indicate $p<0.001$, determined using one-way ANOVA. n = 33-35 measurements. **i**. WT,
915 *CEP90*$^{-/-}$ and *MNR*$^{-/-}$ serum-starved RPE1 cells immunostained for Centrobin (yellow), centrioles
916 (FOP, cyan) and distal appendages (CEP164, magenta). Scale bar = 1 μm. **j**. Quantification of
917 whether Centrobin localizes to one or two centrioles. n>50 cells from two biological replicates.
918 CEP90 and MNR are not required to remove Centrobin from the distal mother centriole. **k**. WT,
919 *CEP90*$^{-/-}$ and *MNR*$^{-/-}$ serum-starved RPE1 cells immunostained for CEP120 (yellow), centrioles
920 (FOP, cyan) and distal appendages (CEP164, magenta). Scale bar = 1 μm. **j**. Quantification of
921 whether CEP120 localizes to one or two centrioles. n>50 cells from two biological replicates.
922 CEP90 and MNR are not required to remove Centrobin or CEP120 from the distal mother
923 centriole.

924

925 **REFERENCES**

926 Andersen, J.S., C.J. Wilkinson, T. Mayor, P. Mortensen, E.A. Nigg, and M. Mann. 2003. Proteomic
927 characterization of the human centrosome by protein correlation profiling. *Nature*. 426:570–
928 574. doi:10.1038/nature02166.

929 Bowler, M., D. Kong, S. Sun, R. Nanjundappa, L. Evans, V. Farmer, A. Holland, M.R. Mahjoub,
930 H. Sui, and J. Loncarek. 2019. High-resolution characterization of centriole distal appendage
931 morphology and dynamics by correlative STORM and electron microscopy. *Nat. Commun.*
932 10. doi:10.1038/s41467-018-08216-4.

933 Breslow, D.K., and A.J. Holland. 2019. Mechanism and Regulation of Centriole and Cilium
934 Biogenesis. *Annu. Rev. Biochem.* 88:691–724. doi:10.1146/annurev-biochem-013118-
935 111153.

936 Chevrier, V., A.-L. Bruel, T.J.P. Van Dam, B. Franco, M. Lo Scalzo, F. Lembo, S. Audebert, E.
937 Baudelet, D. Isnardon, A. Bole, J.-P. Borg, P. Kuentz, J. Thevenon, L. Burglen, L. Faivre, J.-
938 B. Rivière, M.A. Huynen, D. Birnbaum, O. Rosnet, and C. Thauvin-Robinet. 2016.
939 OFIP/KIAA0753 forms a complex with OFD1 and FOR20 at pericentriolar satellites and
940 centrosomes and is mutated in one individual with oral-facial-digital syndrome. *Hum. Mol.*
941 *Genet.* 25:497–513. doi:10.1093/hmg/ddv488.

942 Chong, W.M., W.-J. Wang, C.-H. Lo, T.-Y. Chiu, T.-J. Chang, Y.-P. Liu, B. Tanos, G. Mazo, M.-
943 F.B. Tsou, W.-N. Jane, T.T. Yang, and J.-C. Liao. 2020. Super-resolution microscopy reveals
944 coupling between mammalian centriole subdistal appendages and distal appendages. *Elife*.
945 9. doi:10.7554/elife.53580.

946 Ciccarelli, F.D., T. Doerks, C. Von Mering, C.J. Creevey, B. Snel, and P. Bork. 2006. Toward
947 automatic reconstruction of a highly resolved tree of life. *Science (80-.).* 311:1283–1287.
948 doi:10.1126/science.1123061.

949 Coene, K.L.M., R. Roepman, D. Doherty, B. Afroze, H.Y. Kroes, S.J.F. Letteboer, L.H. Ngu, B.
950 Budny, E. van Wijk, N.T. Gorden, M. Azhimi, C. Thauvin-Robinet, J.A. Veltman, M. Boink, T.
951 Kleefstra, F.P.M. Cremers, H. van Bokhoven, and A.P.M. de Brouwer. 2009. OFD1 Is
952 Mutated in X-Linked Joubert Syndrome and Interacts with LCA5-Encoded Lebercilin. *Am. J.*
953 *Hum. Genet.* 85:465–481. doi:10.1016/j.ajhg.2009.09.002.

954 Corbit, K.C., P. Aanstad, V. Singla, A.R. Norman, D.Y.R. Stainier, and J.F. Reiter. 2005.
955 Vertebrate Smoothened functions at the primary cilium. *Nature*. 437:1018–1021.
956 doi:10.1038/nature04117.

957 Cox, J., and M. Mann. 2008. MaxQuant enables high peptide identification rates, individualized
958 p.p.b.-range mass accuracies and proteome-wide protein quantification. *Nat. Biotechnol.*
959 26:1367–1372. doi:10.1038/nbt.1511.

960 Deutsch, E.W., A. Csordas, Z. Sun, A. Jarnuczak, Y. Perez-Riverol, T. Ternent, D.S. Campbell,
961 M. Bernal-Llinares, S. Okuda, S. Kawano, R.L. Moritz, J.J. Carver, M. Wang, Y. Ishihama,
962 N. Bandeira, H. Hermjakob, and J.A. Vizcaíno. 2017. The ProteomeXchange consortium in
963 2017: Supporting the cultural change in proteomics public data deposition. *Nucleic Acids*
964 *Res.* 45:D1100–D1106. doi:10.1093/nar/gkw936.

965 Feng, S., Y. Song, M. Shen, S. Xie, W. Li, Y. Lu, Y. Yang, G. Ou, J. Zhou, F. Wang, W. Liu, X.
966 Yan, X. Liang, and T. Zhou. 2017. Microtubule-binding protein FOR20 promotes microtubule
967 depolymerization and cell migration. *Cell Discov.* 3:1–13. doi:10.1038/celldisc.2017.32.

968 Goehring, N.W., and A.A. Hyman. 2012. Organelle growth control through limiting pools of
969 cytoplasmic components. *Curr. Biol.* 22:R330–R339. doi:10.1016/j.cub.2012.03.046.

970 Gönczy, P. 2015. Centrosomes and cancer: Revisiting a long-standing relationship. *Nat. Rev.*
971 *Cancer*. 15:639–652. doi:10.1038/nrc3995.

972 Hammarsjö, A., Z. Wang, R. Vaz, F. Taylan, M. Sedghi, K.M. Girisha, D. Chitayat, K.
973 Neethukrishna, P. Shannon, R. Godoy, K. Gowrishankar, A. Lindstrand, J. Nasiri, M.
974 Baktashian, P.T. Newton, L. Guo, W. Hofmeister, M. Pettersson, A.S. Chagin, G. Nishimura,
975 L. Yan, N. Matsumoto, A. Nordgren, N. Miyake, G. Grigelioniene, and S. Ikegawa. 2017.
976 Novel KIAA0753 mutations extend the phenotype of skeletal ciliopathies. *Sci. Rep.* 7.
977 doi:10.1038/s41598-017-15442-1.

978 Hebbar, M., A. Kanthi, A. Shukla, S. Bielas, and K.M. Girisha. 2018. A biallelic 36-bp insertion in
979 PIBF1 is associated with Joubert syndrome. *J. Hum. Genet.* 63:935–939.
980 doi:10.1038/s10038-018-0462-7.

981 Hori, A., and T. Toda. 2017. Regulation of centriolar satellite integrity and its physiology. *Cell. Mol.*
982 *Life Sci.* 74:213–229. doi:10.1007/s00018-016-2315-x.

983 Huangfu, D., A. Liu, A.S. Rakeman, N.S. Murcia, L. Niswander, and K. V. Anderson. 2003.

984 Hedgehog signalling in the mouse requires intraflagellar transport proteins. *Nature*. 426:83–
985 87. doi:10.1038/nature02061.

986 Hunkapiller, J., V. Singla, A. Seol, and J.F. Reiter. 2011. The ciliogenic protein oral-facial-digital
987 1 regulates the neuronal differentiation of embryonic stem cells. *Stem Cells Dev.* 20:831–
988 841. doi:10.1089/scd.2010.0362.

989 Ibrahim, R., C. Messaoudi, F.J. Chichon, C. Celati, and S. Marco. 2009. Electron tomography
990 study of isolated human centrioles. *Microsc. Res. Tech.* 72:42–48. doi:10.1002/jemt.20637.

991 Jakobsen, L., K. Vanselow, M. Skogs, Y. Toyoda, E. Lundberg, I. Poser, L.G. Falkenby, M.
992 Bennetzen, J. Westendorf, E.A. Nigg, M. Uhlen, A.A. Hyman, and J.S. Andersen. 2011.
993 Novel asymmetrically localizing components of human centrosomes identified by
994 complementary proteomics methods. *EMBO J.* 30:1520–1535. doi:10.1038/emboj.2011.63.

995 Keller, L.C., S. Geimer, E. Romijn, J. Yates, I. Zamora, and W.F. Marshall. 2009. Molecular
996 architecture of the centriole proteome: The conserved WD40 domain protein POC1 is
997 required for centriole duplication and length control. *Mol. Biol. Cell*. 20:1150–1166.
998 doi:10.1091/mbc.E08-06-0619.

999 Keller, L.C., E.P. Romijn, I. Zamora, J.R. Yates, and W.F. Marshall. 2005. Proteomic analysis of
1000 isolated Chlamydomonas centrioles reveals orthologs of ciliary-disease genes. *Curr. Biol.*
1001 15:1090–1098. doi:10.1016/j.cub.2005.05.024.

1002 Kim, K., K. Lee, and K. Rhee. 2012. CEP90 Is Required for the Assembly and Centrosomal
1003 Accumulation of Centriolar Satellites, Which Is Essential for Primary Cilia Formation. *PLoS*
1004 *One*. 7:e48196. doi:10.1371/journal.pone.0048196.

1005 Kim, K., and K. Rhee. 2011. The pericentriolar satellite protein CEP90 is crucial for integrity of the
1006 mitotic spindle pole. *J. Cell Sci.* 124:338–347. doi:10.1242/jcs.078329.

1007 Kodani, A., T.W. Yu, J.R. Johnson, D. Jayaraman, T.L. Johnson, L. Al-Gazali, L. Sztriha, J.N.
1008 Partlow, H. Kim, A.L. Krup, A. Dammermann, N.J. Krogan, C.A. Walsh, and J.F. Reiter. 2015.
1009 Centriolar satellites assemble centrosomal microcephaly proteins to recruit CDK2 and
1010 promote centriole duplication. *Elife*. 4:e07519. doi:10.7554/eLife.07519.

1011 Kong, D., N. Sahabandu, C. Sullenberger, A. Vásquez-Limeta, D. Luvsanjav, K. Lukasik, and J.
1012 Loncarek. 2020. Prolonged mitosis results in structurally aberrant and over-elongated
1013 centrioles. *J. Cell Biol.* 219. doi:10.1083/jcb.201910019.

1014 Lu, Q., C. Insinna, C. Ott, J. Stauffer, P.A. Pintado, J. Rahajeng, U. Baxa, V. Walia, A. Cuenca,
1015 Y.S. Hwang, I.O. Daar, S. Lopes, J. Lippincott-Schwartz, P.K. Jackson, S. Caplan, and C.J.
1016 Westlake. 2015. Early steps in primary cilium assembly require EHD1/EHD3-dependent
1017 ciliary vesicle formation. *Nat. Cell Biol.* 17:228–240. doi:10.1038/ncb3109.

1018 Mahjoub, M.R., Z. Xie, and T. Stearns. 2010. Cep120 is asymmetrically localized to the daughter
1019 centriole and is essential for centriole assembly. *J. Cell Biol.* 191:331–346.
1020 doi:10.1083/jcb.201003009.

1021 Marteil, G., A. Guerrero, A.F. Vieira, B.P. De Almeida, P. Machado, S. Mendonça, M. Mesquita,
1022 B. Villarreal, I. Fonseca, M.E. Francia, K. Dores, N.P. Martins, S.C. Jana, E.M. Tranfield,
1023 N.L. Barbosa-Morais, J. Paredes, D. Pellman, S.A. Godinho, and M. Bettencourt-Dias. 2018.
1024 Over-elongation of centrioles in cancer promotes centriole amplification and chromosome
1025 missegregation. *Nat. Commun.* 9:1–17. doi:10.1038/s41467-018-03641-x.

1026 Mazo, G., N. Soplop, W.-J. Wang, K. Uryu, and M.-F. Bryan Tsou. 2016. Spatial Control of Primary
1027 Ciliogenesis by Subdistal Appendages Alters Sensation-Associated Properties of Cilia
1028 Developmental Cell Spatial Control of Primary Ciliogenesis by Subdistal Appendages Alters
1029 Sensation-Associated Properties of Cilia. *Dev. Cell*. 39:424–437.
1030 doi:10.1016/j.devcel.2016.10.006.

1031 McQuin, C., A. Goodman, V. Chernyshev, L. Kamentsky, B.A. Cimini, K.W. Karhohs, M. Doan, L.
1032 Ding, S.M. Rafelski, D. Thirstrup, W. Wiegraebe, S. Singh, T. Becker, J.C. Caicedo, and A.E.
1033 Carpenter. 2018. CellProfiler 3.0: Next-generation image processing for biology. *PLOS Biol.*
1034 16:e2005970. doi:10.1371/JOURNAL.PBIO.2005970.

1035 Meier, F., A.D. Brunner, S. Koch, H. Koch, M. Lubeck, M. Krause, N. Goedecke, J. Decker, T.
1036 Kosinski, M.A. Park, N. Bache, O. Hoerning, J. Cox, O. Räther, and M. Mann. 2018. Online
1037 parallel accumulation–serial fragmentation (PASEF) with a novel trapped ion mobility mass
1038 spectrometer. *Mol. Cell. Proteomics*. 17:2534–2545. doi:10.1074/mcp.TIR118.000900.

1039 Nigg, E.A., and A.J. Holland. 2018. Once and only once: Mechanisms of centriole duplication and
1040 their deregulation in diseases. *Nat. Rev. Mol. Cell Biol.* 19:297–312.
1041 doi:10.1038/nrm.2017.127.

1042 Odabasi, E., S. Gul, I.H. Kavakli, and E.N. Firat-Karalar. 2019. Centriolar satellites are required
1043 for efficient ciliogenesis and ciliary content regulation. *EMBO Rep.* 20.
1044 doi:10.15252/embr.201947723.

1045 Paintrand, M., M. Moudjou, H. Delacroix, and M. Bornens. 1992. Centrosome organization and
1046 centriole architecture: Their sensitivity to divalent cations. *J. Struct. Biol.* 108:107–128.
1047 doi:10.1016/1047-8477(92)90011-X.

1048 Perez-Riverol, Y., A. Csordas, J. Bai, M. Bernal-Llinares, S. Hewapathirana, D.J. Kundu, A.
1049 Inuganti, J. Griss, G. Mayer, M. Eisenacher, E. Pérez, J. Uszkoreit, J. Pfeuffer, T.
1050 Sachsenberg, Ş. Yilmaz, S. Tiwary, J. Cox, E. Audain, M. Walzer, A.F. Jarnuczak, T.
1051 Ternent, A. Brazma, and J.A. Vizcaíno. 2019. The PRIDE database and related tools and
1052 resources in 2019: Improving support for quantification data. *Nucleic Acids Res.* 47:D442–
1053 D450. doi:10.1093/nar/gky1106.

1054 Prianichnikov, N., H. Koch, S. Koch, M. Lubeck, R. Heilig, S. Brehmer, R. Fischer, and J. Cox.
1055 2020. Maxquant software for ion mobility enhanced shotgun proteomics. *Mol. Cell.*
1056 *Proteomics*. 19:1058–1069. doi:10.1074/mcp.TIR119.001720.

1057 Prosser, S.L., and L. Pelletier. 2020. Centriolar satellite biogenesis and function in vertebrate
1058 cells. *J. Cell Sci.* 133. doi:10.1242/jcs.239566.

1059 Reiter, J.F., and M.R. Leroux. 2017. Genes and molecular pathways underpinning ciliopathies.
1060 *Nat. Rev. Mol. Cell Biol.* 18:533–547. doi:10.1038/nrm.2017.60.

1061 Schmidt, K.N., S. Kuhns, A. Neuner, B. Hub, H. Zentgraf, and G. Pereira. 2012a. Cep164
1062 mediates vesicular docking to the mother centriole during early steps of ciliogenesis. *J. Cell*
1063 *Biol.* 199:1083–1101. doi:10.1083/jcb.201202126.

1064 Schmidt, K.N., S. Kuhns, A. Neuner, B. Hub, H. Zentgraf, and G. Pereira. 2012b. Cep164
1065 mediates vesicular docking to the mother centriole during early steps of ciliogenesis. *J. Cell*
1066 *Biol.* 199:1083–1101. doi:10.1083/jcb.201202126.

1067 Schneider, C.A., W.S. Rasband, and K.W. Eliceiri. 2012. NIH Image to ImageJ: 25 years of image
1068 analysis. *Nat. Methods*. 9:671–675. doi:10.1038/nmeth.2089.

1069 Shen, Y., H. Wang, Z. Liu, M. Luo, S. Ma, C. Lu, Z. Cao, Y. Yu, R. Cai, C. Chen, Q. Li, H. Gao,
1070 Y. Peng, B. Xu, and X. Ma. 2020. Identification of two novel pathogenic variants of PIBF1 by
1071 whole exome sequencing in a 2-year-old boy with Joubert syndrome. *BMC Med. Genet.*
1072 21:192. doi:10.1186/s12881-020-01130-x.

1073 Shi, X., G. Garcia, J.C. Van De Weghe, R. McGorty, G.J. Pazour, D. Doherty, B. Huang, and J.F.
1074 Reiter. 2017. Super-resolution microscopy reveals that disruption of ciliary transition-zone

1075 architecture causes Joubert syndrome. *Nat. Cell Biol.* 19:1178–1188. doi:10.1038/ncb3599.

1076 Shi, X., Q. Li, Z. Dai, A. Tran, S. Feng, A.D. Ramirez, Z. Lin, X. Wang, T.T. Chow, I.B. Seiple, and
1077 B. Huang. 2019. Label-retention expansion microscopy. *bioRxiv*. 687954.
1078 doi:10.1101/687954.

1079 Sillibourne, J.E., I. Hurbain, T. Grand-Perret, B. Goud, P. Tran, and M. Bornens. 2013. Primary
1080 ciliogenesis requires the distal appendage component Cep123. *Biol. Open*. 2:535–545.
1081 doi:10.1242/bio.20134457.

1082 Singla, V., M. Romaguera-Ros, J.M. Garcia-Verdugo, and J.F. Reiter. 2010. Ofd1, a Human
1083 Disease Gene, Regulates the Length and Distal Structure of Centrioles. *Dev. Cell*. 18:410–
1084 424. doi:10.1016/j.devcel.2009.12.022.

1085 Srivastava, S., and D. Panda. 2017. A centrosomal protein FOR20 regulates microtubule
1086 assembly dynamics and plays a role in cell migration. *Biochem. J.* 474:2841–2859.
1087 doi:10.1042/BCJ20170303.

1088 Stephen, J., T. Vilboux, L. Mian, C. Kuptanon, C.M. Sinclair, D. Yildirimli, D.M. Maynard, J. Bryant,
1089 R. Fischer, M. Vemulapalli, J.C. Mullikin, M. Huizing, W.A. Gahl, M.C. V. Malicdan, and M.
1090 Gunay-Aygun. 2017. Mutations in KIAA0753 cause Joubert syndrome associated with
1091 growth hormone deficiency. *Hum. Genet.* 136:399–408. doi:10.1007/s00439-017-1765-z.

1092 Tanos, B.E., H.J. Yang, R. Soni, W.J. Wang, F.P. Macaluso, J.M. Asara, and M.F.B. Tsou. 2013.
1093 Centriole distal appendages promote membrane docking, leading to cilia initiation. *Genes*
1094 *Dev.* 27:163–168. doi:10.1101/gad.207043.112.

1095 Teo, G., G. Liu, J. Zhang, A.I. Nesvizhskii, A.C. Gingras, and H. Choi. 2014. SAINTexpress:
1096 Improvements and additional features in Significance Analysis of INTeractome software. *J.*
1097 *Proteomics*. 100:37–43. doi:10.1016/j.jprot.2013.10.023.

1098 Thauvin-Robinet, C., J.S. Lee, E. Lopez, V. Herranz-Pérez, T. Shida, B. Franco, L. Jego, F. Ye,
1099 L. Pasquier, P. Loget, N. Gigot, B. Aral, C.A.M. Lopes, J. St-Onge, A.L. Bruel, J. Thevenon,
1100 S. González-Granero, C. Alby, A. Munnich, M. Vekemans, F. Huet, A.M. Fry, S. Saunier,
1101 J.B. Rivière, T. Attié-Bitach, J.M. Garcia-Verdugo, L. Faivre, A. Mégarbané, and M. V.
1102 Nachury. 2014. The oral-facial-digital syndrome gene C2CD3 encodes a positive regulator
1103 of centriole elongation. *Nat. Genet.* 46:905–911. doi:10.1038/ng.3031.

1104 Tsai, J.J., W. Bin Hsu, J.H. Liu, C.W. Chang, and T.K. Tang. 2019. CEP120 interacts with C2CD3

1105 and Talpid3 and is required for centriole appendage assembly and ciliogenesis. *Sci. Rep.*
1106 9:1–15. doi:10.1038/s41598-019-42577-0.

1107 Viol, L., S. Hata, A. Pastor-Peidro, A. Neuner, F. Murke, P. Wuchter, A.D. Ho, B. Giebel, and G.
1108 Pereira. 2020. Nek2 kinase displaces distal appendages from the mother centriole prior to
1109 mitosis. *J. Cell Biol.* 219. doi:10.1083/jcb.201907136.

1110 Wang, L., M. Failler, W. Fu, and B.D. Dynlacht. 2018. A distal centriolar protein network controls
1111 organelle maturation and asymmetry. *Nat. Commun.* 9. doi:10.1038/s41467-018-06286-y.

1112 Wang, L., K. Lee, R. Malonis, I. Sanchez, and B.D. Dynlacht. 2016. Tethering of an E3 ligase by
1113 PCM1 regulates the abundance of centrosomal KIAA0586/Talpid3 and promotes
1114 ciliogenesis. *Elife*. 5. doi:10.7554/eLife.12950.

1115 Wassie, A.T., Y. Zhao, and E.S. Boyden. 2019. Expansion microscopy: principles and uses in
1116 biological research. *Nat. Methods*. 16:33–41. doi:10.1038/s41592-018-0219-4.

1117 Westlake, C.J., L.M. Baye, M. V. Nachury, K.J. Wright, K.E. Ervin, L. Phu, C. Chalouni, J.S. Beck,
1118 D.S. Kirkpatrick, D.C. Slusarski, V.C. Sheffield, R.H. Scheller, and P.K. Jackson. 2011.
1119 Primary cilia membrane assembly is initiated by Rab11 and transport protein particle II
1120 (TRAPPII) complex-dependent trafficking of Rabin8 to the centrosome. *Proc. Natl. Acad. Sci.*
1121 *U. S. A.* 108:2759–2764. doi:10.1073/pnas.1018823108.

1122 Wheway, G., M. Schmidts, D.A. Mans, K. Szymanska, T.-M.T. Nguyen, H. Racher, I.G. Phelps,
1123 G. Toedt, J. Kennedy, K.A. Wunderlich, N. Sorusch, Z.A. Abdelhamed, S. Natarajan, W.
1124 Herridge, J. van Reeuwijk, N. Horn, K. Boldt, D.A. Parry, S.J.F. Letteboer, S. Roosing, M.
1125 Adams, S.M. Bell, J. Bond, J. Higgins, E.E. Morrison, D.C. Tomlinson, G.G. Slaats, T.J.P.
1126 van Dam, L. Huang, K. Kessler, A. Giessl, C. V. Logan, E.A. Boyle, J. Shendure, S. Anazi,
1127 M. Aldahmesh, S. Al Hazzaa, R.A. Hegele, C. Ober, P. Frosk, A.A. Mhanni, B.N. Chodirker,
1128 A.E. Chudley, R. Lamont, F.P. Bernier, C.L. Beaulieu, P. Gordon, R.T. Pon, C. Donahue,
1129 A.J. Barkovich, L. Wolf, C. Toomes, C.T. Thiel, K.M. Boycott, M. McKibbin, C.F. Inglehearn,
1130 F. Stewart, H. Omran, M.A. Huynen, P.I. Sergouniotis, F.S. Alkuraya, J.S. Parboosingh, A.M.
1131 Innes, C.E. Willoughby, R.H. Giles, A.R. Webster, M. Ueffing, O. Blacque, J.G. Gleeson, U.
1132 Wolfrum, P.L. Beales, T. Gibson, D. Doherty, H.M. Mitchison, R. Roepman, and C.A.
1133 Johnson. 2015. An siRNA-based functional genomics screen for the identification of
1134 regulators of ciliogenesis and ciliopathy genes. *Nat. Cell Biol.* 17:1074–1087.
1135 doi:10.1038/ncb3201.

1136 Winey, M., and E. O'Toole. 2014. Centriole structure. *Philos. Trans. R. Soc. B Biol. Sci.* 369.
1137 doi:10.1098/rstb.2013.0457.

1138 Wu, C.T., H.Y. Chen, and T.K. Tang. 2018. Myosin-Va is required for preciliary vesicle
1139 transportation to the mother centriole during ciliogenesis. *Nat. Cell Biol.* 20:175–185.
1140 doi:10.1038/s41556-017-0018-7.

1141 Yang, T.T., W.M. Chong, W.J. Wang, G. Mazo, B. Tanos, Z. Chen, T.M.N. Tran, Y. De Chen,
1142 R.R. Weng, C.E. Huang, W.N. Jane, M.F.B. Tsou, and J.C. Liao. 2018. Super-resolution
1143 architecture of mammalian centriole distal appendages reveals distinct blade and matrix
1144 functional components. *Nat. Commun.* 9:1–11. doi:10.1038/s41467-018-04469-1.

1145 Ye, X., H. Zeng, G. Ning, J.F. Reiter, and A. Liu. 2014. C2cd3 is critical for centriolar distal
1146 appendage assembly and ciliary vesicle docking in mammals. *Proc. Natl. Acad. Sci. U. S. A.*
1147 111:2164–2169. doi:10.1073/pnas.1318737111.

1148 Zimmermann, L., A. Stephens, S.Z. Nam, D. Rau, J. Kübler, M. Lozajic, F. Gabler, J. Söding, A.N.
1149 Lupas, and V. Alva. 2018. A Completely Reimplemented MPI Bioinformatics Toolkit with a
1150 New HHpred Server at its Core. *J. Mol. Biol.* 430:2237–2243. doi:10.1016/j.jmb.2017.12.007.

1151

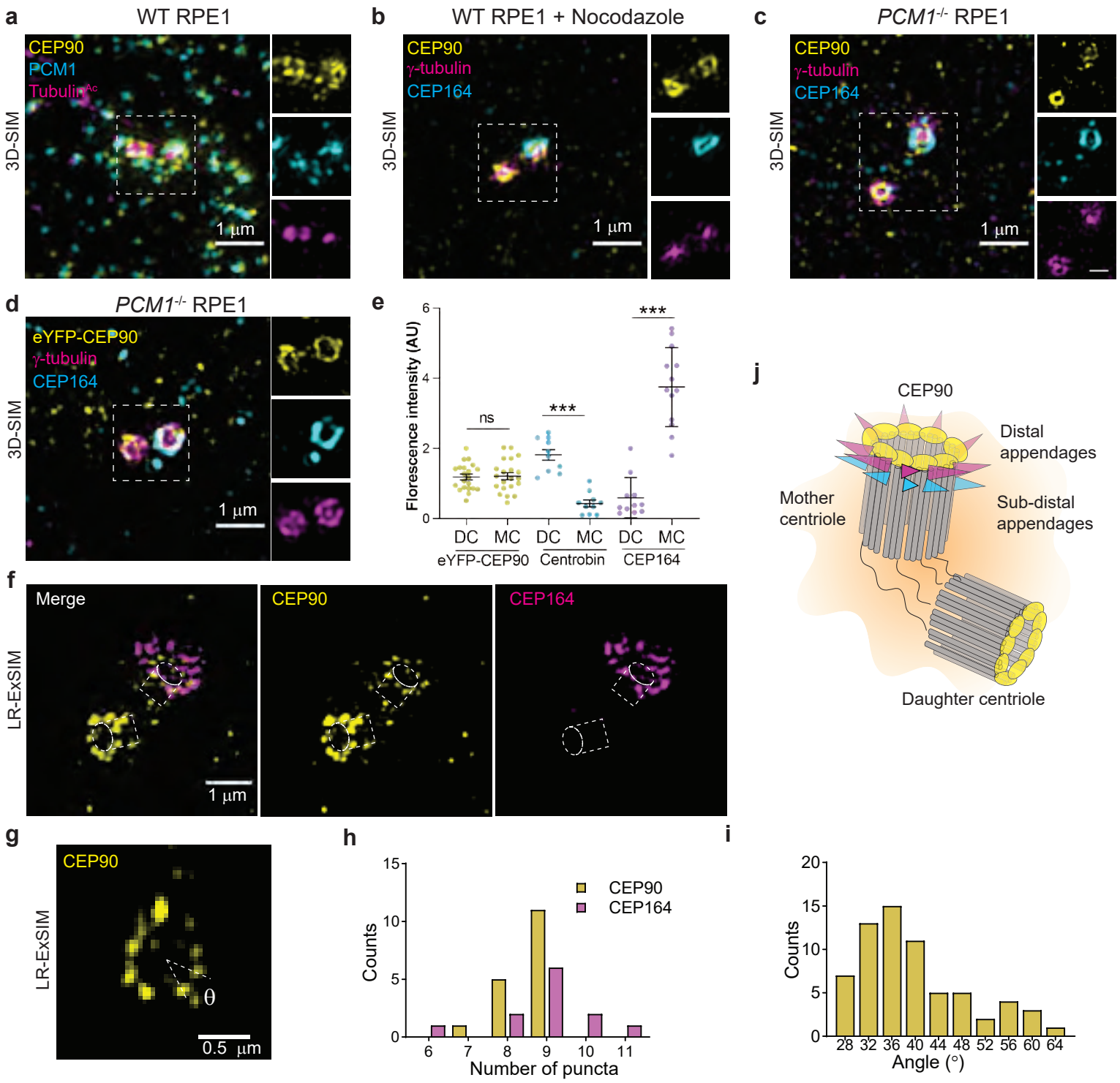
a
WT RPE1
3D-SIM
CEP90
PCM1
Tubulin Ac
1 µm
b
WT RPE1 + Nocodazole
3D-SIM
CEP90
γ-tubulin
CEP164
1 µm
c
PCM1-/- RPE1
3D-SIM
CEP90
γ-tubulin
CEP164
1 µm
d
PCM1-/- RPE1
3D-SIM
eYFP-CEP90
γ-tubulin
CEP164
1 µm
e
Florescence intensity (AU)
ns
***
***
DC MC DC MC DC MC
eYFP-CEP90 Centrobin CEP164
j
CEP90
Distal appendages
Mother centriole
Sub-distal appendages
Daughter centriole
f
LR-ExSIM
Merge
CEP90
CEP164
1 µm
g
LR-ExSIM
CEP90
θ
0.5 µm
h
Counts
CEP90
CEP164
Number of puncta
i
Counts
Angle (°)

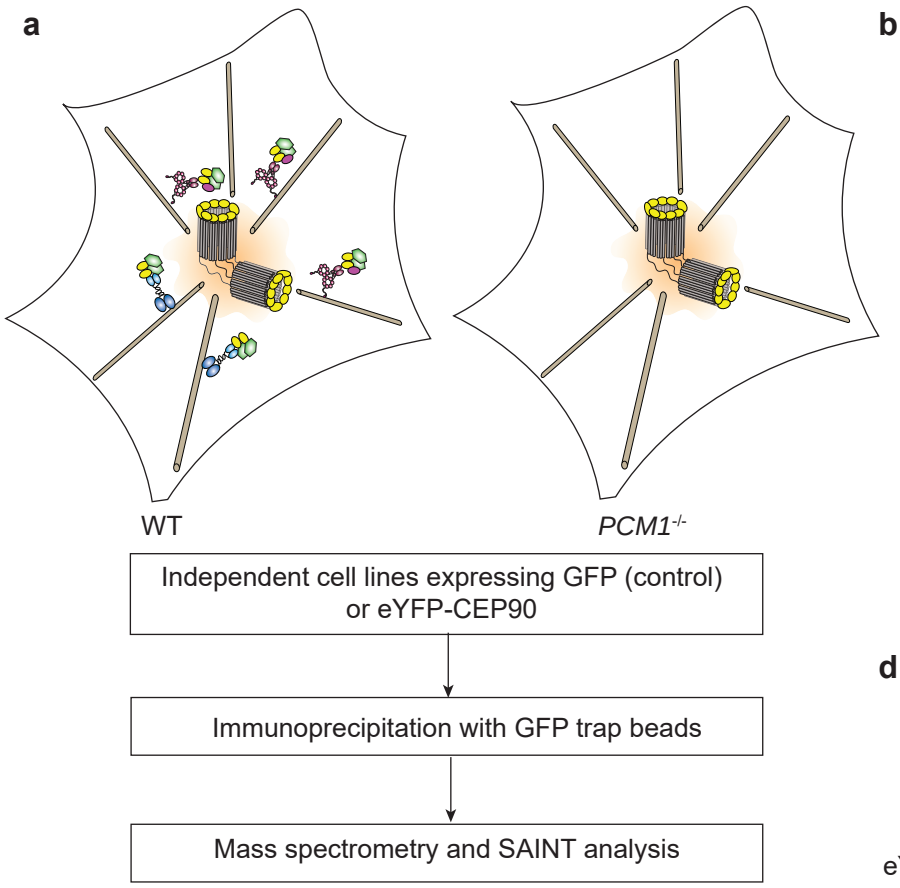
a
WT
PCM1-/-
Independent cell lines expressing GFP (control) or eYFP-CEP90
Immunoprecipitation with GFP trap beads
Mass spectrometry and SAINT analysis

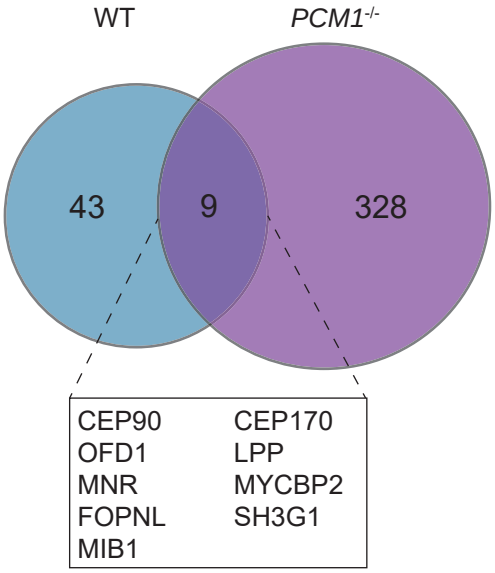
b
WT
PCM1-/-
43
9
328
CEP90
OFD1
MNR
FOPNL
MIB1
CEP170
LPP
MYCBP2
SH3G1

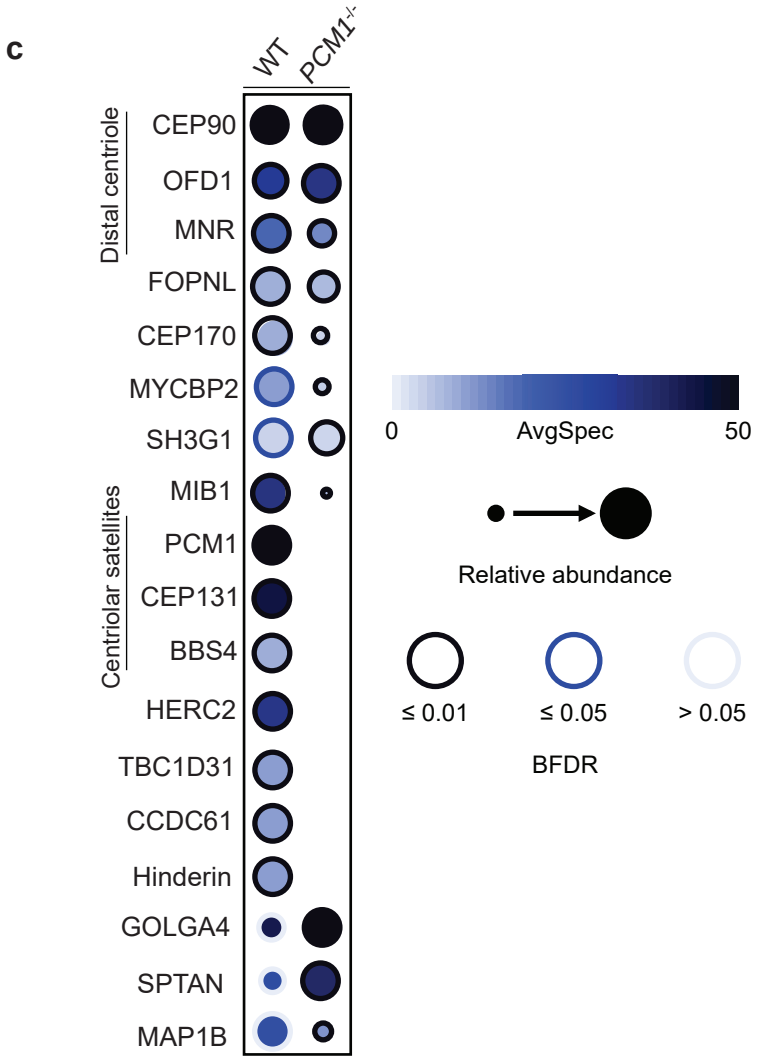
c
WT
PCM1-/-
Distal centriole
CEP90
OFD1
MNR
FOPNL
CEP170
MYCBP2
SH3G1
Centriolar satellites
MIB1
PCM1
CEP131
BBS4
HERC2
TBC1D31
CCDC61
Hinderin
GOLGA4
SPTAN
MAP1B
0
AvgSpec
50
Relative abundance
≤ 0.01
≤ 0.05
> 0.05
BFDR

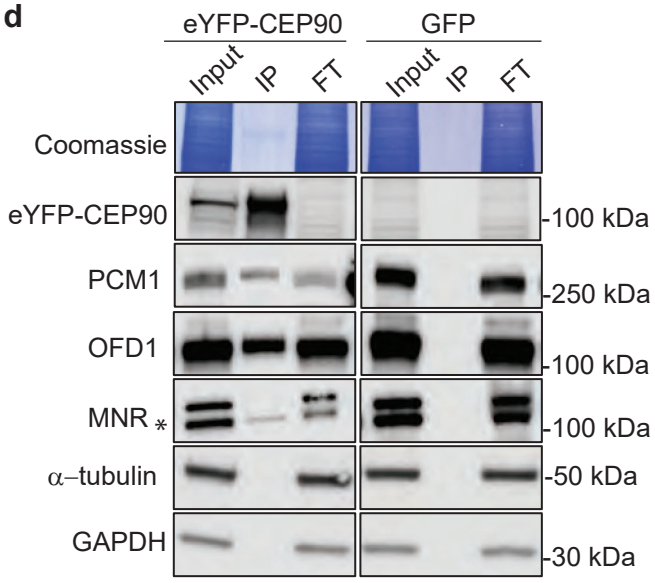
d
eYFP-CEP90
GFP
Input
IP
FT
Input
IP
FT
Coomassie
eYFP-CEP90
PCM1
OFD1
MNR *
α–tubulin
GAPDH
100 kDa
250 kDa
100 kDa
100 kDa
50 kDa
30 kDa

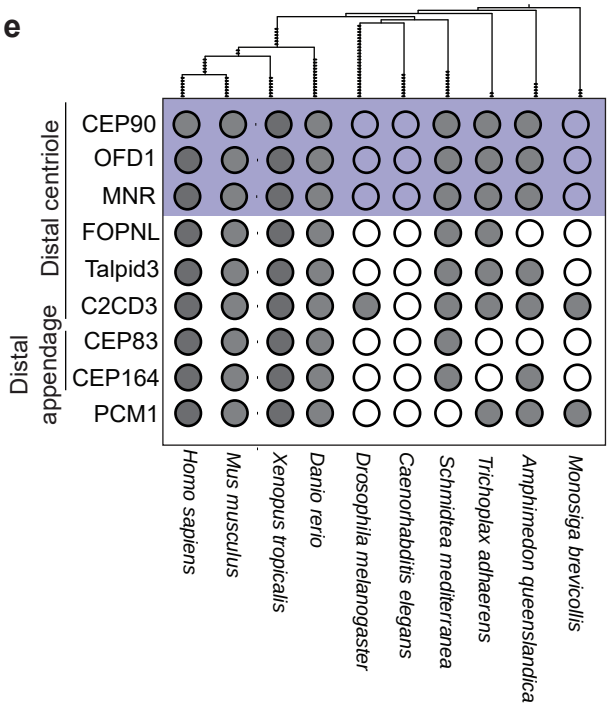
e
Distal centriole
CEP90
OFD1
MNR
Distal appendage
FOPNL
Talpid3
C2CD3
CEP83
CEP164
PCM1
Homo sapiens
Mus musculus
Xenopus tropicalis
Danio rerio
Drosophila melanogaster
Caenorhabditis elegans
Schmidtea mediterranea
Trichoplax adhaerens
Amphimedon queenslandica
Monosiga brevicollis

and at the distal centriole

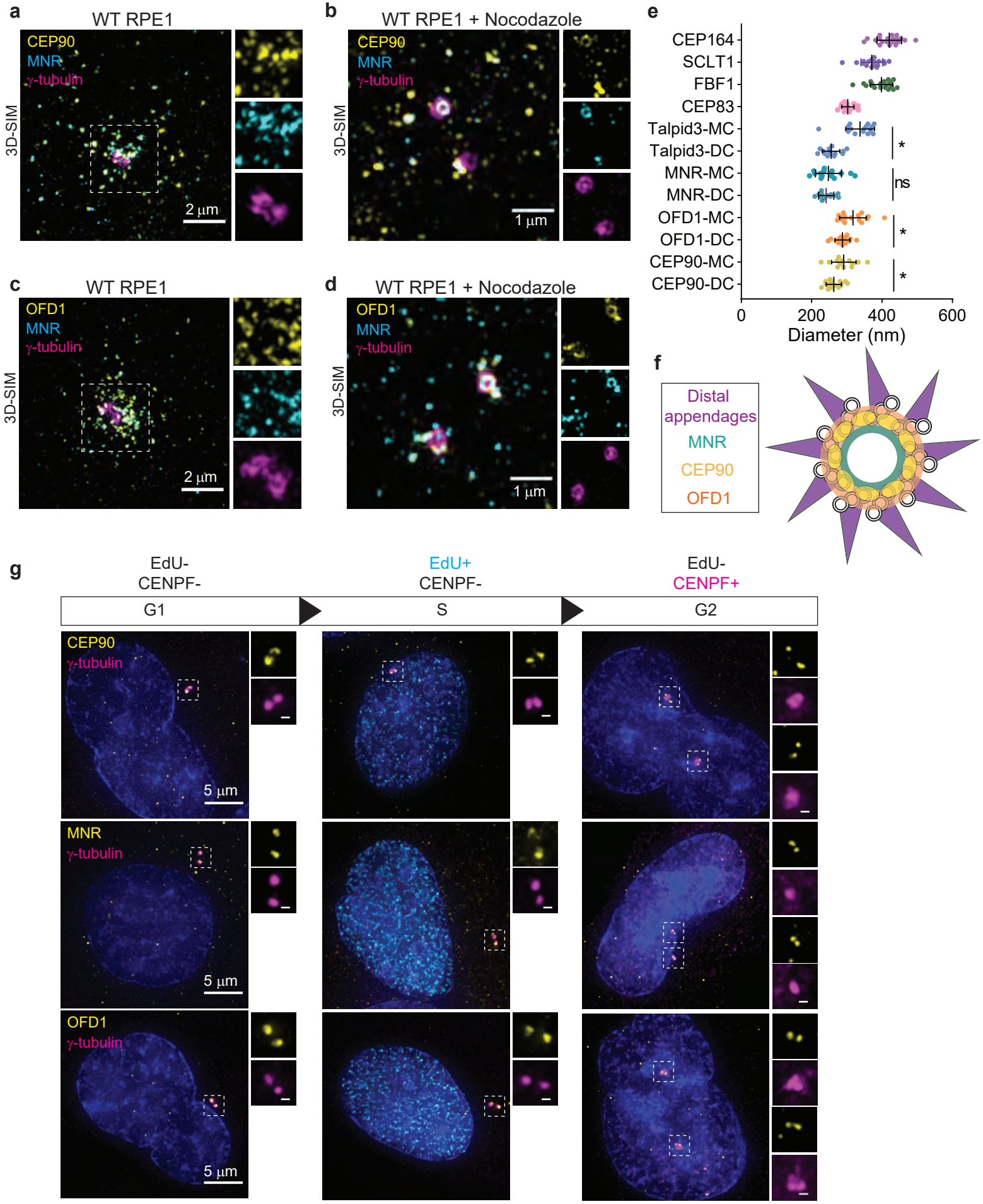

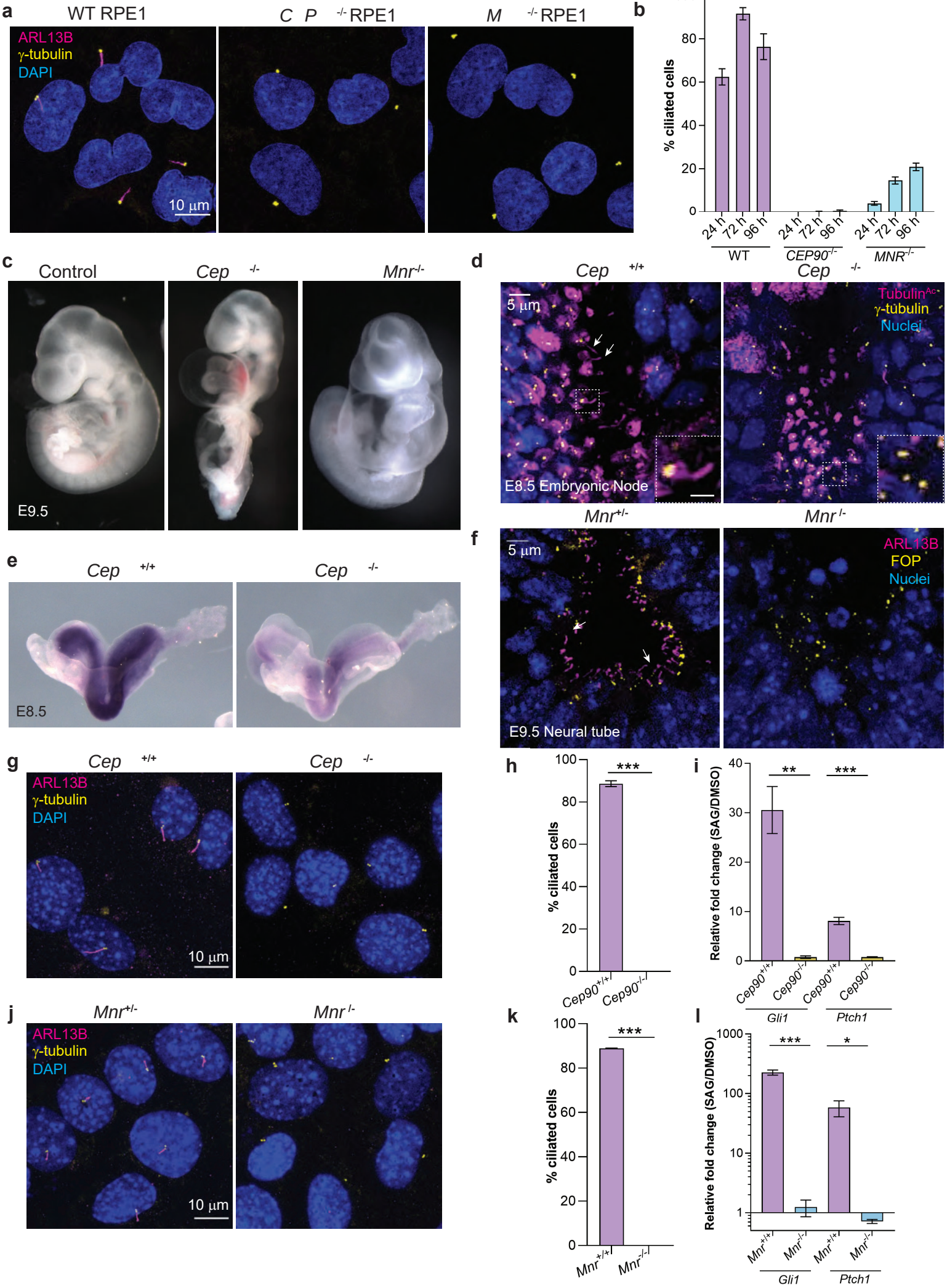
a
WT RPE1
C P -/- RPE1
M -/- RPE1
ARL13B
γ-tubulin
DAPI
10 μm
b
% ciliated cells
0
20
40
60
80
24 h
72 h
96 h
WT
CEP90-/-
MNR-/-
c
Control
Cep -/-
Mnr-/-
E9.5
d
Cep +/+
Cep -/-
5 μm
TubulinAc
γ-tubulin
Nuclei
E8.5 Embryonic Node
e
Cep +/+
Cep -/-
E8.5
f
Mnr+/-
Mnr -/-
5 μm
ARL13B
FOP
Nuclei
E9.5 Neural tube
g
Cep +/+
Cep -/-
ARL13B
γ-tubulin
DAPI
10 μm
h
% ciliated cells
***
Cep90+/+
Cep90-/-
i
Relative fold change (SAG/DMSO)
**
***
Cep90+/+
Cep90-/-
Gli1
Ptch1
j
Mnr+/-
Mnr -/-
ARL13B
γ-tubulin
DAPI
10 μm
k
% ciliated cells
***
Mnr+/+
Mnr-/-
l
Relative fold change (SAG/DMSO)
***
*
Mnr+/+
Mnr-/-
Gli1
Ptch1

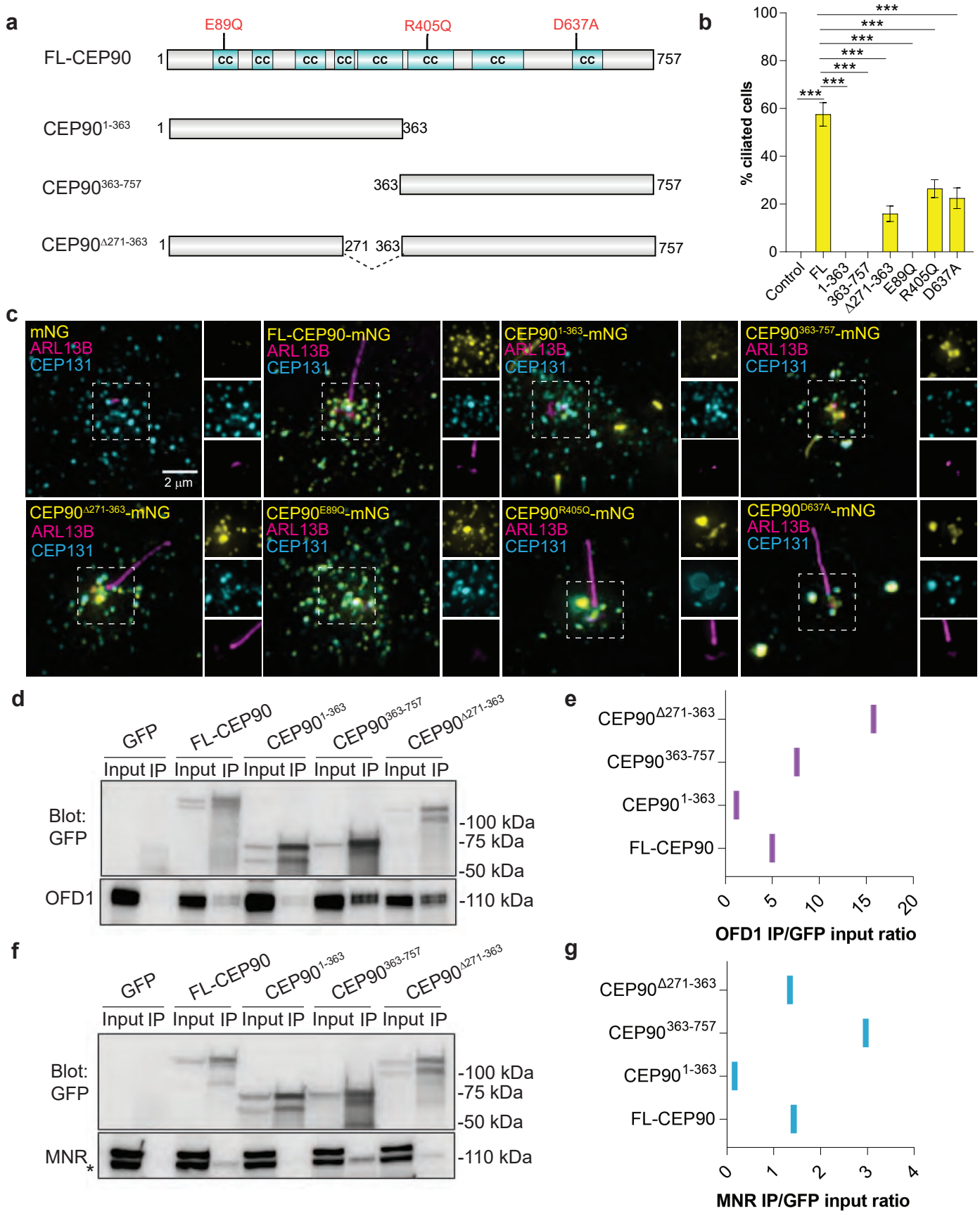
a
E89Q
R405Q
D637A
FL-CEP90
CEP90 1-363
CEP90 363-757
CEP90 Δ271-363
cc
1
757
363
271
b
% ciliated cells
Control
FL
1-363
363-757
Δ271-363
E89Q
R405Q
D637A
c
mNG
ARL13B
CEP131
2 µm
FL-CEP90-mNG
CEP90 1-363-mNG
CEP90 363-757-mNG
CEP90 Δ271-363-mNG
CEP90 E89Q-mNG
CEP90 R405Q-mNG
CEP90 D637A-mNG
d
GFP
FL-CEP90
CEP90 1-363
CEP90 363-757
CEP90 Δ271-363
Input IP
Blot: GFP
OFD1
-100 kDa
-75 kDa
-50 kDa
-110 kDa
e
OFD1 IP/GFP input ratio
f
MNR*
g
MNR IP/GFP input ratio

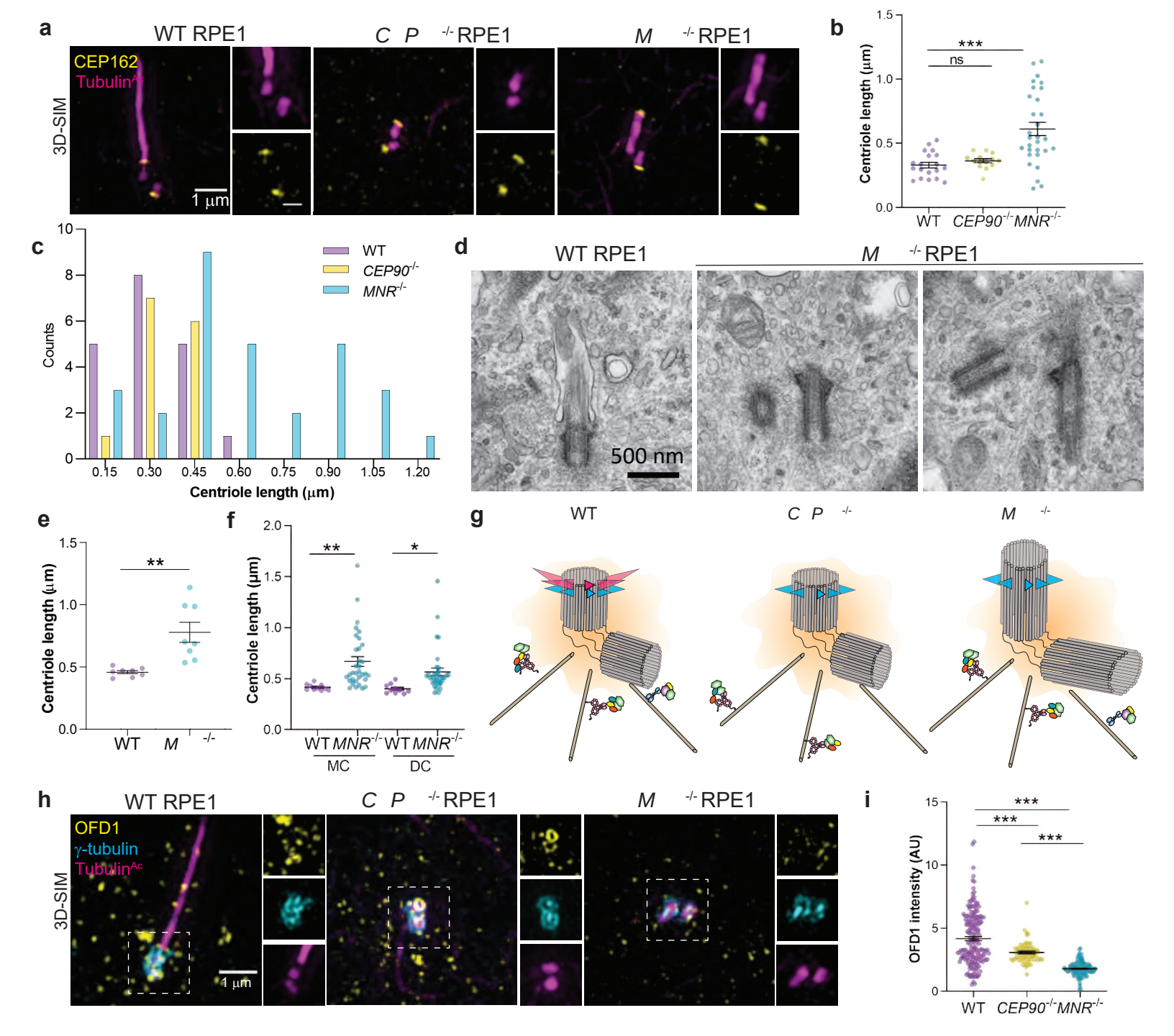
a
WT RPE1
CEP162
Tubulin^Ac
3D-SIM
1 µm
CP -/- RPE1
M -/- RPE1
b
Centriole length (µm)
***
ns
WT
CEP90-/-
MNR-/-
c
Counts
WT
CEP90-/-
MNR-/-
Centriole length (µm)
d
WT RPE1
M -/- RPE1
500 nm
e
Centriole length (µm)
**
WT
M -/-
f
Centriole length (µm)
**
*
WT MNR-/- WT MNR-/-
MC
DC
g
WT
CP -/-
M -/-
h
WT RPE1
CP -/- RPE1
M -/- RPE1
OFD1
γ-tubulin
Tubulin^Ac
3D-SIM
1 µm
i
OFD1 intensity (AU)
***
***
***
WT
CEP90-/-
MNR-/-

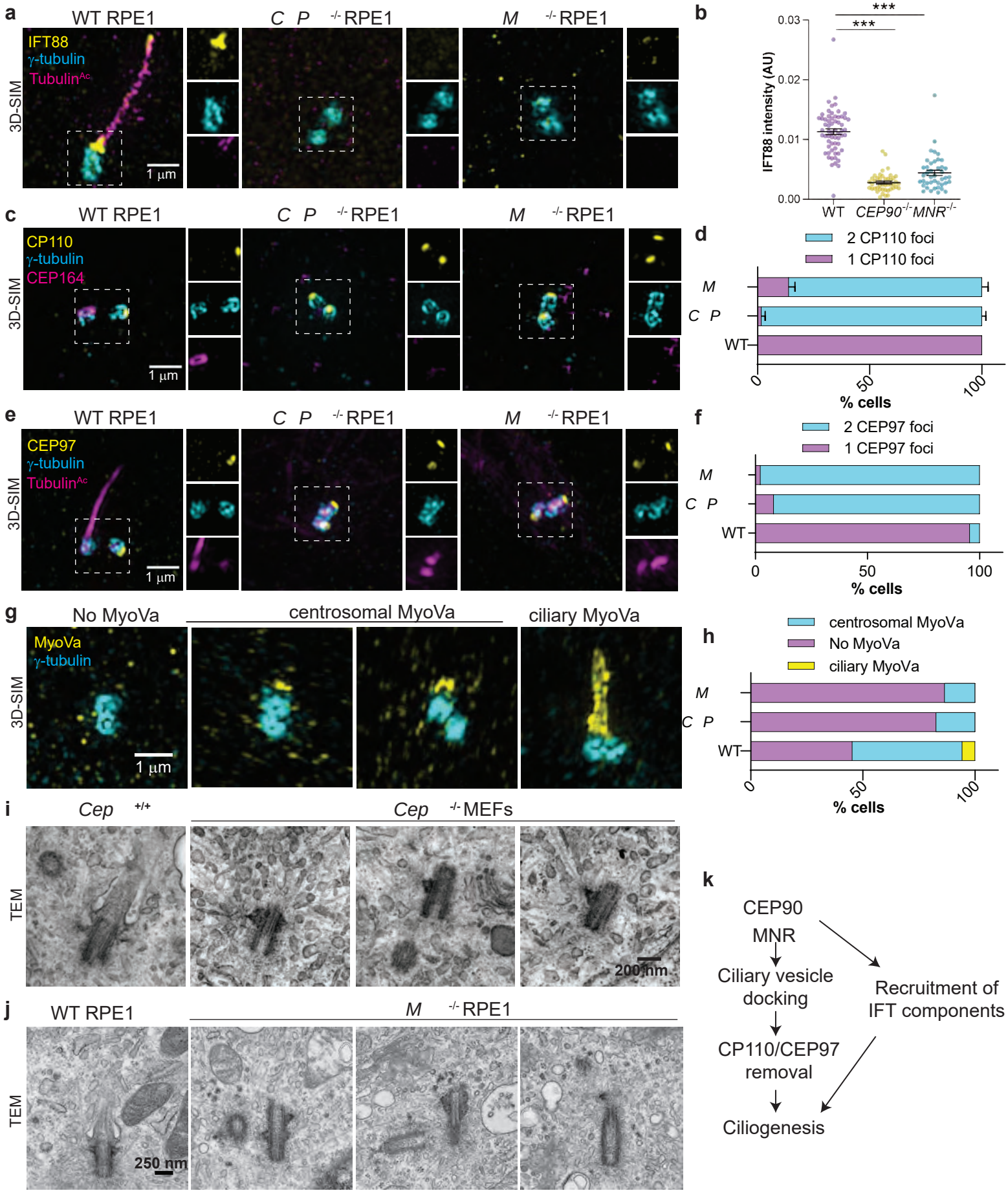
a
WT RPE1
C P -/- RPE1
M -/- RPE1
3D-SIM
IFT88
γ-tubulin
TubulinAc
1 µm
b
***
***
IFT88 intensity (AU)
0.03
0.02
0.01
0.00
WT
CEP90-/-
MNR-/-
c
WT RPE1
C P -/- RPE1
M -/- RPE1
3D-SIM
CP110
γ-tubulin
CEP164
1 µm
d
2 CP110 foci
1 CP110 foci
M
C P
WT
0
50
100
% cells
e
WT RPE1
C P -/- RPE1
M -/- RPE1
3D-SIM
CEP97
γ-tubulin
TubulinAc
1 µm
f
2 CEP97 foci
1 CEP97 foci
M
C P
WT
0
50
100
% cells
g
No MyoVa
centrosomal MyoVa
ciliary MyoVa
3D-SIM
MyoVa
γ-tubulin
1 µm
h
centrosomal MyoVa
No MyoVa
ciliary MyoVa
M
C P
WT
0
50
100
% cells
i
Cep +/+
Cep -/- MEFs
TEM
200 nm
j
WT RPE1
M -/- RPE1
TEM
250 nm
k
CEP90
MNR
Ciliary vesicle docking
CP110/CEP97 removal
Ciliogenesis
Recruitment of IFT components

components to the mother centriole.

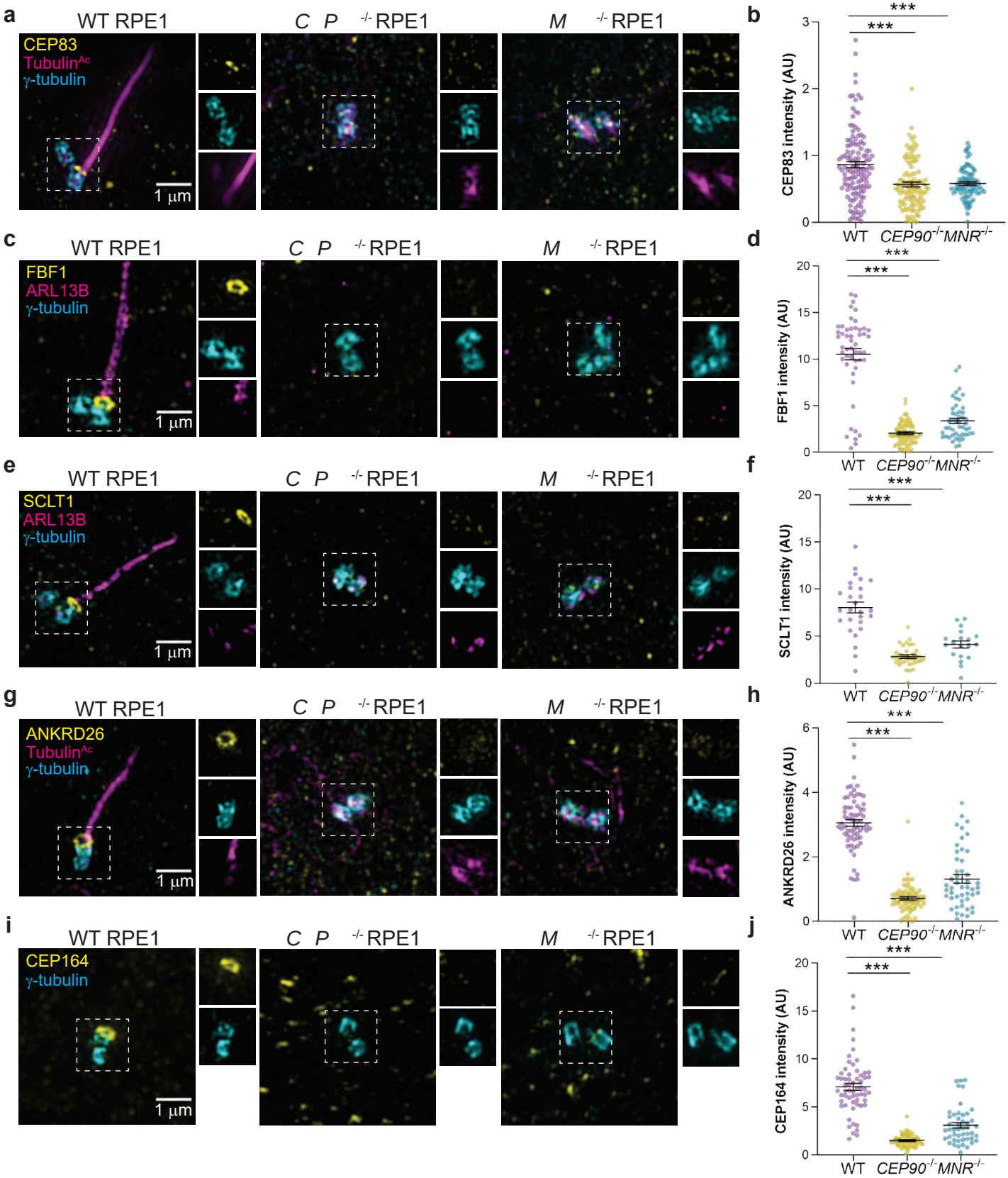

at the mother centriole

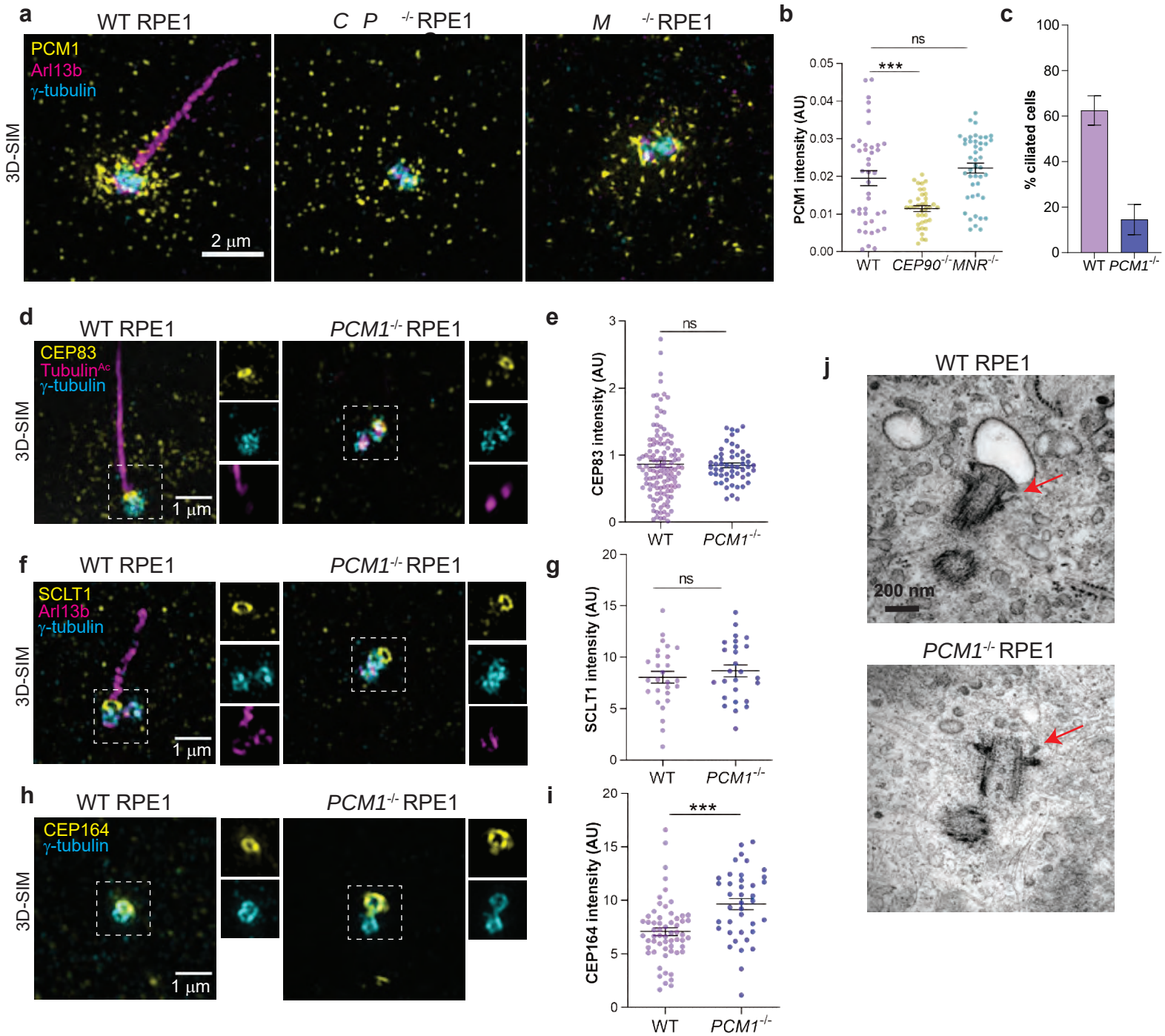

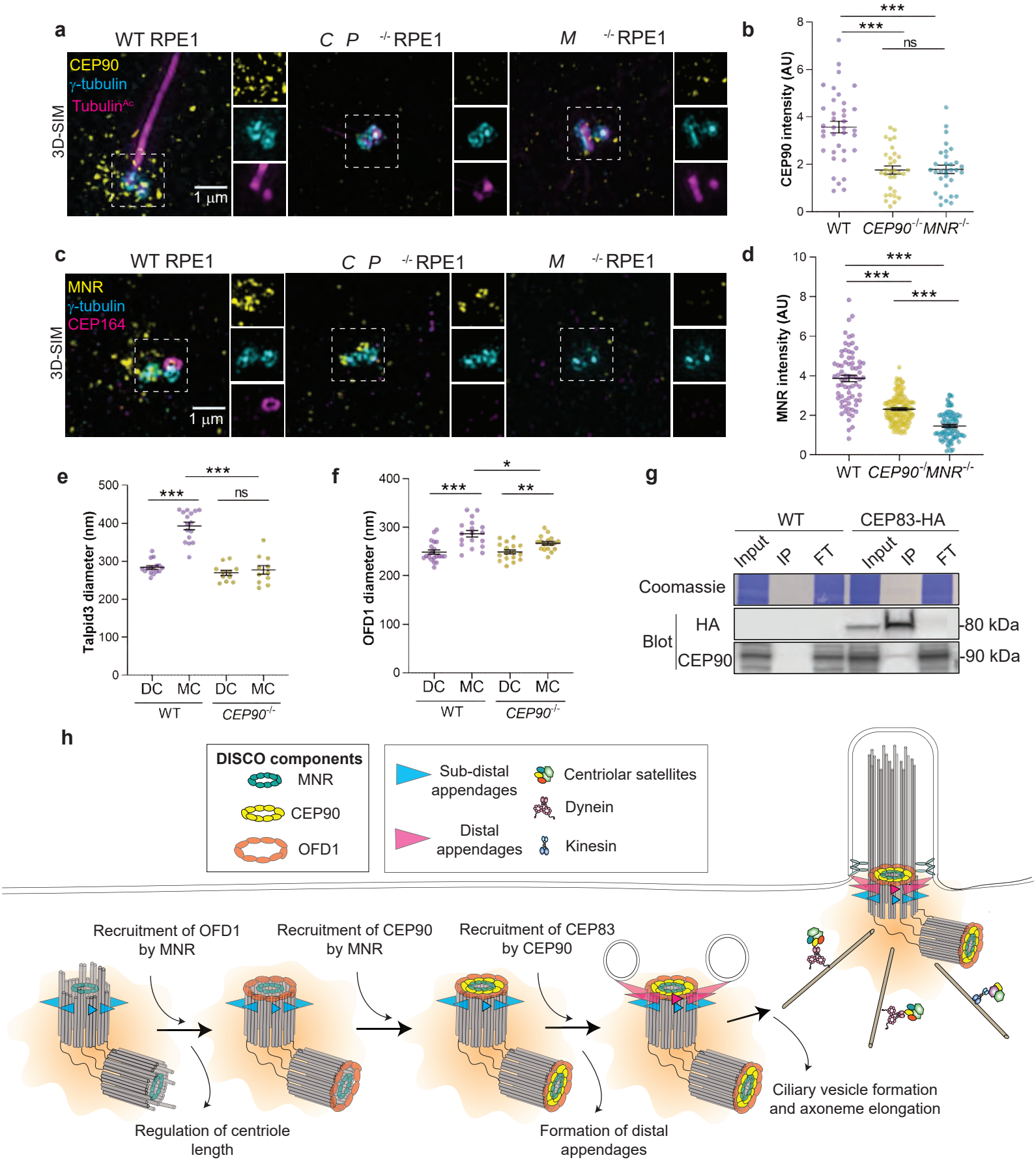
a
WT RPE1
C P -/- RPE1
M -/- RPE1
3D-SIM
CEP90
γ-tubulin
Tubulin^Ac
1 µm
b
CEP90 intensity (AU)
***
***
ns
WT
CEP90-/-
MNR-/-
c
WT RPE1
C P -/- RPE1
M -/- RPE1
3D-SIM
MNR
γ-tubulin
CEP164
1 µm
d
MNR intensity (AU)
***
***
***
WT
CEP90-/-
MNR-/-
e
Talpid3 diameter (nm)
***
***
ns
DC
MC
DC
MC
WT
CEP90-/-
f
OFD1 diameter (nm)
*
***
**
DC
MC
DC
MC
WT
CEP90-/-
g
WT
CEP83-HA
Input
IP
FT
Input
IP
FT
Coomassie
Blot
HA
CEP90
-80 kDa
-90 kDa
h
DISCO components
MNR
CEP90
OFD1
Sub-distal appendages
Distal appendages
Centriolar satellites
Dynein
Kinesin
Recruitment of OFD1 by MNR
Recruitment of CEP90 by MNR
Recruitment of CEP83 by CEP90
Regulation of centriole length
Formation of distal appendages
Ciliary vesicle formation and axoneme elongation

Supplementary Fig 1: Generation of *CEP90*$^{-/-}$, *MNR*$^{-/-}$ and *PCM1*$^{-/-}$ RPE1 cell lines

a

C P $^{+/+}$ allele: 5'- TAGTTTAGAAACAACAGTTCCTACGGATGATATTTCCTCATCAGAAGAG -3'
C P $^{+/+}$ translate : MSRKISKESKKVNISSSLESEDISLETTVPTDDISSSEEREGKVRI----

C P $^{-/-}$ allele 1: 5'- TAGTTTAGAAACAACAGTTCCTA--|GATGATATTTCCTCATCAGAAGAG -3'
C P $^{-/-}$ allele 1 translate: MSRKISKESKKVNISSSLESEDISLETTVPR*

C P $^{-/-}$ allele 2: 5'- TAGTTTAGAAACAACAGTTCCTACG|--TGATATTTCCTCATCAGAAGAG -3'
C P $^{-/-}$ allele 2 translate: MSRKISKESKKVNISSSLESEDISLETTVPT*

b

M $^{+/+}$ allele: 5'- TTTGATTCCTTCCTTTCCACCCTGTGTCGGGTATTTTATACTTAGTATGTC -3'
M $^{+/+}$ allele translate: MGPGQ---SSQKCGHTKYKIPDHRVERKESKSQAACQCSHQPSKVEISSSGAKVY----

M $^{-/-}$ allele 1: 5'- TTTGATTCCTTCCTTTCCACCCTGT|-GTCGGGTATTTTATACTTAGTATGTC -3'
M $^{-/-}$ allele 1 translate: MGPGQ---SSQKCGHTKYKIPDTGWKGRNQRVKQPVSVATSHPK*

M $^{-/-}$ allele 2: 5'- TTTGATTCCTTCCTTTCCACCCTGT|NGGTCGGGTATTTTATACTTAGTATGTC -3'
M $^{-/-}$ allele 2 translate:MGPGQ---SSQKCGHTKYKIPDXQGGKEGIKESSSLSV*

c

PCM1$^{+/+}$ allele : 5'- GATCATCAGAAAAGAATAAGAAAAAGTTTGGTGTAGAAAGTGATAAAAGAG -3'
PCM1$^{+/+}$ allele translate: MATGGGPFEDGMNDQDLPNWSNENVDDRLNNMDWGAQQKKANRSSEKNKKKFGVES---

PCM1$^{-/-}$ allele : 5'- GATCATCAGAAAAGAATAAGAAAAA|NGTTTGGTGTAGAAAGTGATAAAAGAG -3'
PCM1$^{-/-}$ allele translate: MATGGGPFEDGMNDQDLPNWSNENVDDRLNNMDWGAQQKKANRSSEKNKKXVWCRK*

PAM site
Cut site
- = deletion
N = insertion
* = stop codon

d

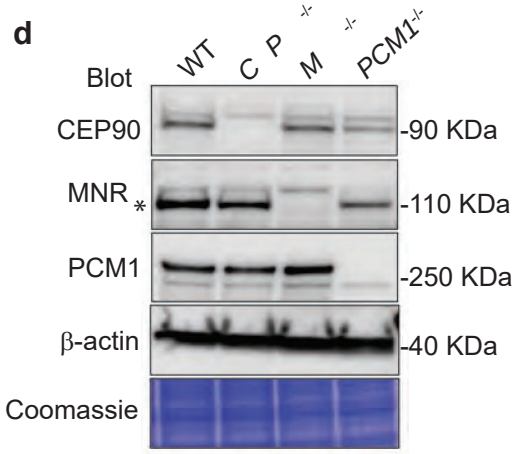

and recruits endogenous OFD1

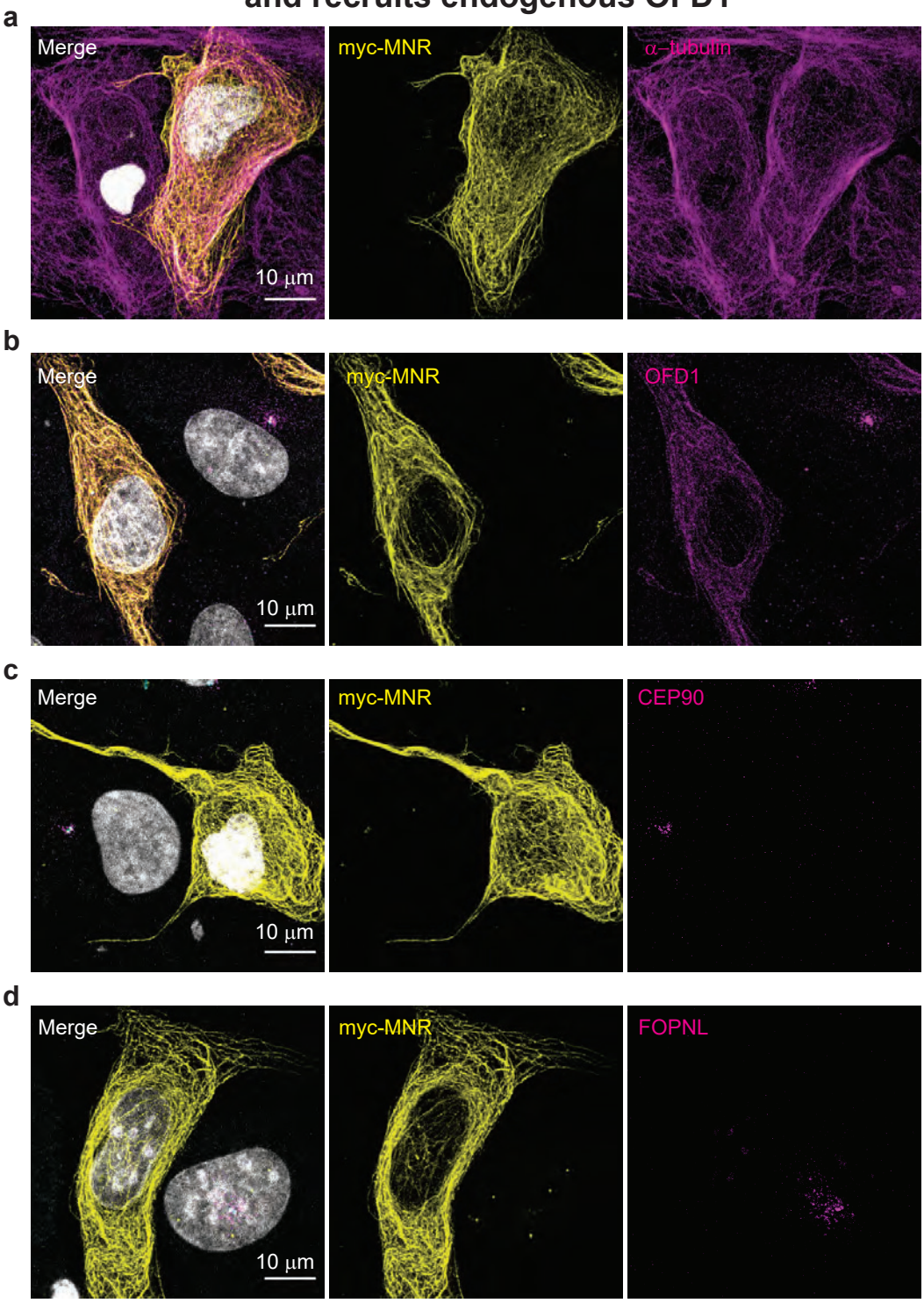

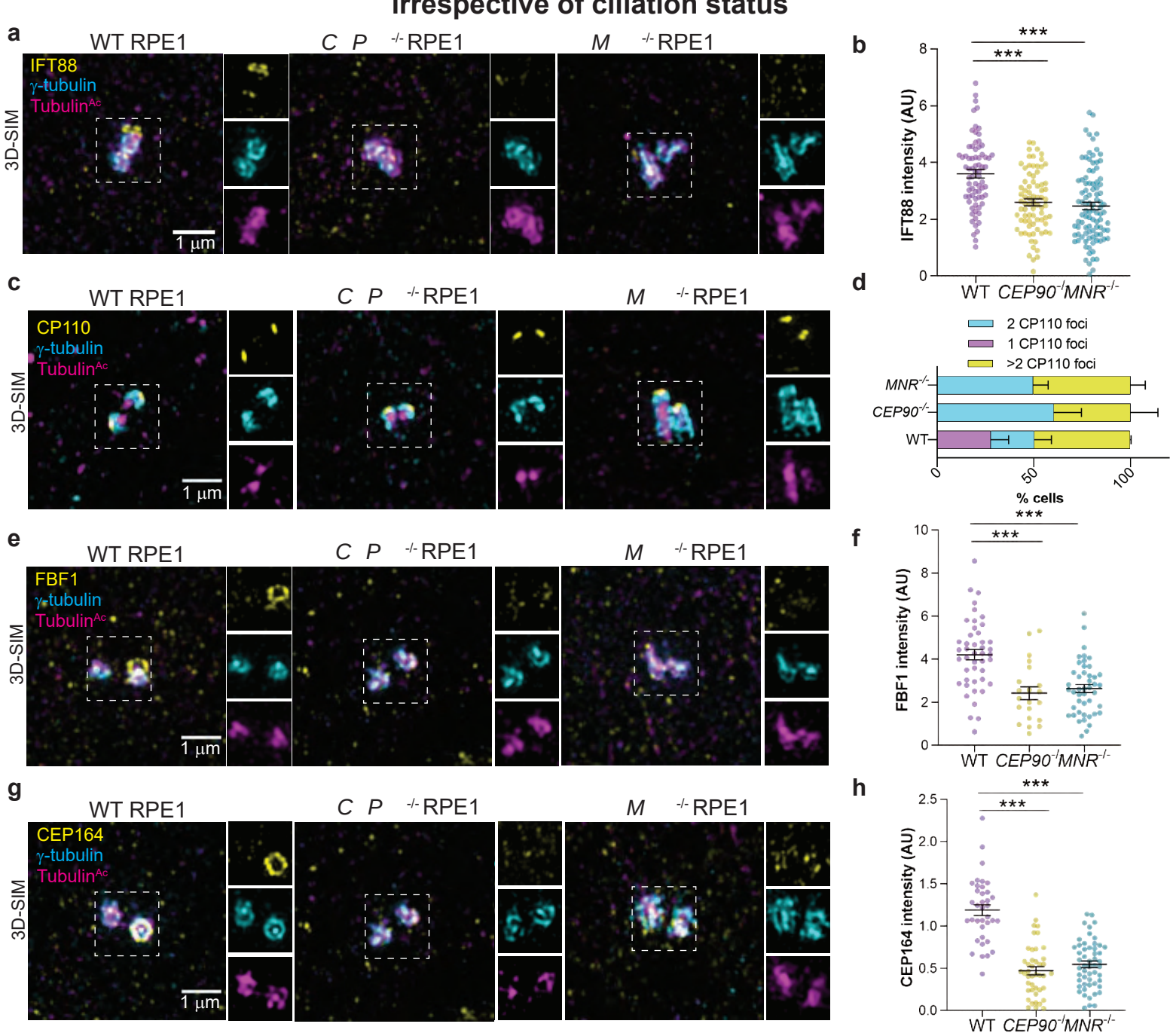

Irrespective of ciliation status
a
WT RPE1
C P -/- RPE1
M -/- RPE1
IFT88
γ-tubulin
TubulinAc
3D-SIM
1 μm
b
IFT88 intensity (AU)
***
***
WT
CEP90-/-
MNR-/-
c
CP110
γ-tubulin
TubulinAc
d
2 CP110 foci
1 CP110 foci
>2 CP110 foci
MNR-/-
CEP90-/-
WT
% cells
e
FBF1
γ-tubulin
TubulinAc
f
FBF1 intensity (AU)
g
CEP164
γ-tubulin
TubulinAc
h
CEP164 intensity (AU)

lacking CEP90 or MNR

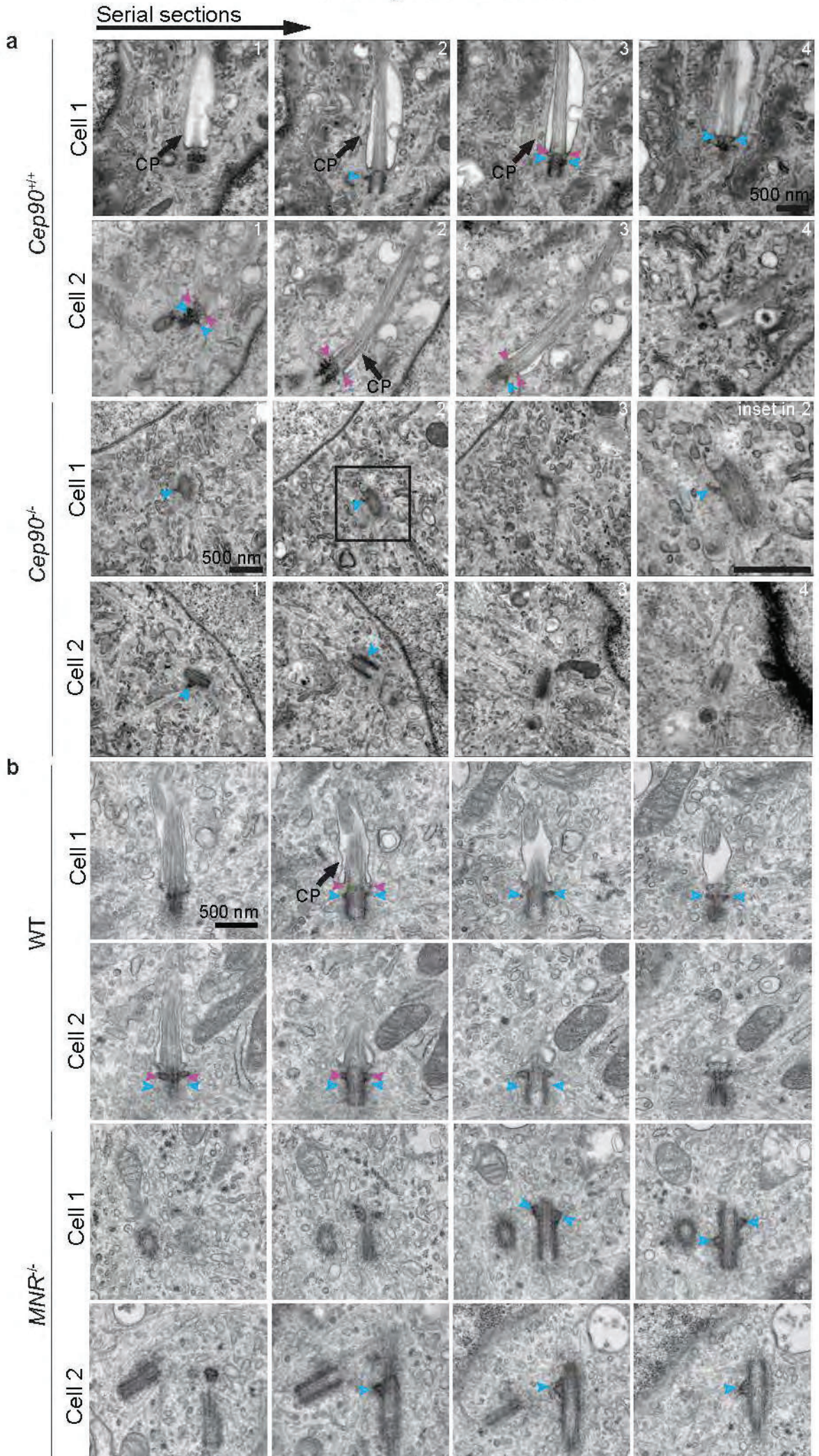

of Talpid3 recruitment and removal of daughter centriole proteins.

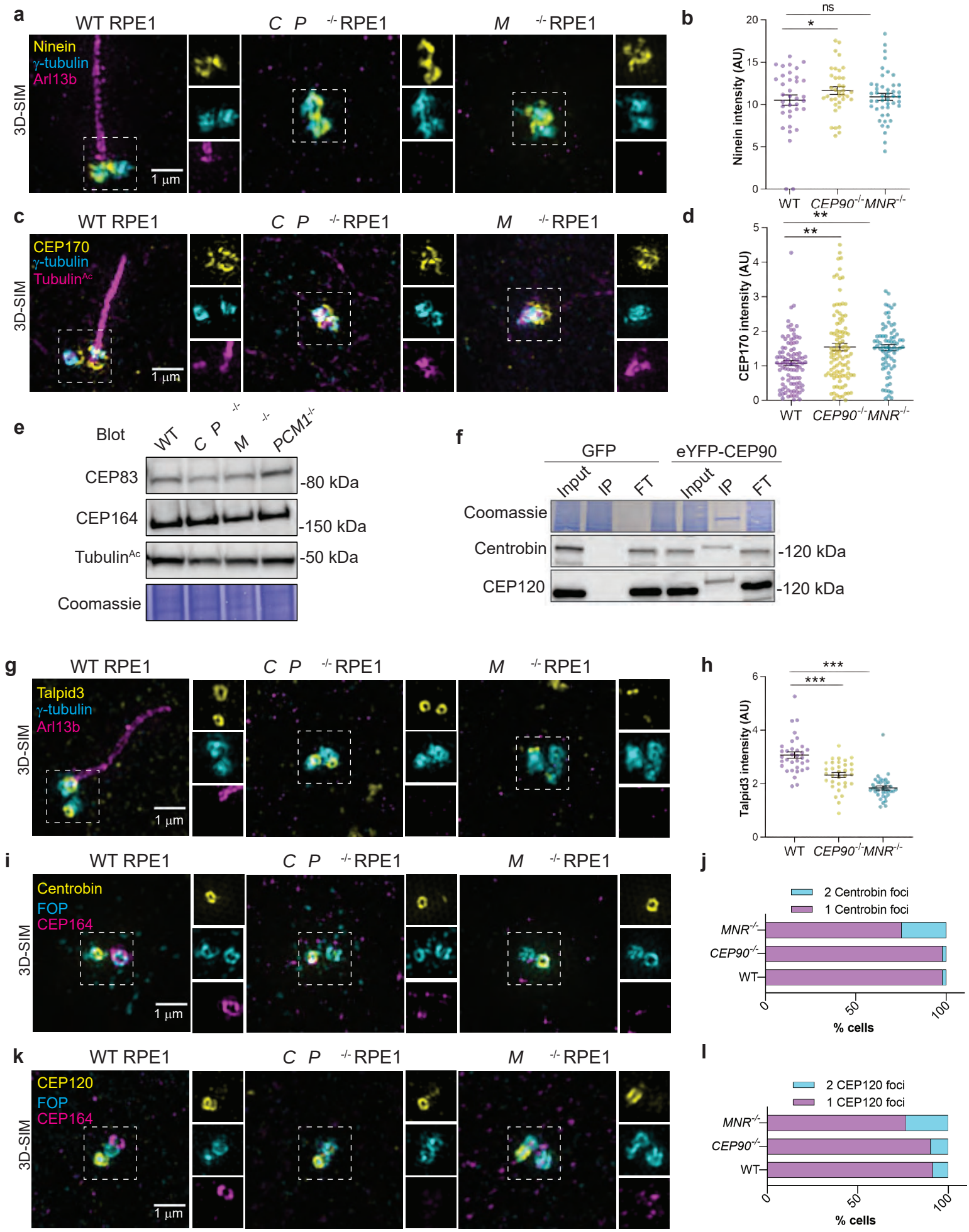

Table 1. List of primary antibodies used in this study for immunofluorescence (IF) and western blotting (WB)

Antibody	Host	Source	Catalog Number	Dilution/Fixation (IF)	Dilution (WB)
CEP90	Rabbit	Proteintech	14413-1-AP		1:500
CEP90	Rabbit	Kunsoo Rhee[1]		1:500/MeOH	
MNR	Rat	Olivier Rosnet[2]		1:500/MeOH	
MNR	Rabbit	Novus Biologicals	NBP1-90929		1:500
OFD1	Rabbit	Novus Biologicals	NBP1-89355	1:500/MeOH	1:500
FOPNL	Rabbit	Sigma Prestige	HPA040599	1:100/MeOH	
CEP164	Goat	Santa Cruz Biotechnology	sc-240226	1:100/MeOH	
CEP164	Mouse	Novus Biologicals	NBP2-43707		1:2000
γ-tubulin	Mouse	Sigma GTU-88	T6557	1:500/MeOH	
Tubulin^{Ac}	Rabbit	Cell Signaling Technology	5335T	1:2000/MeOH	
Tubulin^{Ac}	Mouse	Santa Cruz Biotechnology	sc-23950 AF647	1:100/MeOH	
α-tubulin	Mouse	Sigma Aldrich	T5168	1:1000/PFA	
β-actin	Mouse	Proteintech	6008-1-Ig		1:100,000
GAPDH	Mouse	Proteintech	60004-1-Ig		1:100,000
FBF1	Rabbit	Proteintech	11531-1-AP	1:100/MeOH	
ANKRD26	Rabbit	GeneTex	GTX128255	1:100/MeOH	
CEP83	Rabbit	Sigma Prestige	HPA038161	1:100/MeOH	
CENPF	Mouse	BD Biosciences	610768	1:100/MeOH	
Myo-Va	Rabbit	Novus Biologicals	NBP1-92156	1:100/MeOH	
CP110	Mouse	Millipore	MABT1354	1:100/MeOH	
CEP97	Rabbit	Proteintech	22050-1-AP	1:100/MeOH	
IFT88	Rabbit	Proteintech	13967-1-AP	1:100/MeOH	
FOP	Rabbit	Proteintech	11343-1-AP	1:500/MeOH/ PFA	
PCM1	Rabbit	Proteintech	19856-1-AP		1:500
PCM1	Mouse	Santacruz	sc-398365	1:100/MeOH	
Talpid3	Rabbit	Proteintech	24421-1-AP	1:100/MeOH	
Centrobin	Mouse	Abcam	Ab70448	1:100/MeOH	1:1000
Ninein	Rabbit	Michel Bornens	L79	1:200/MeOH	
ODF2	Mouse	Novus Biologicals	H00004957-M01	1:100/MeOH	
CEP170	Mouse	ThermoFisher	72-413-1	1:100/ MeOH	
Myc-tag	Goat	Novus Biologicals	NB600-335	1:500/PFA	
Arl13b	Rabbit	Proteintech	177100-1-AP	1:500/MeOH/ PFA	
mNeonGreen	Mouse	Chromotek	32F6	1:500/PFA	
Talpid3	Rabbit	Proteintech	24421-1-AP	1:100/MeOH	
CEP162	Rabbit	Sigma Prestige	HPA030170	1:100/MeOH	
CEP131	Guinea pig	Kodani et al.,2015 [3]		1:100/PFA/ MeOH	
CEP120	Rabbit	Betleja et al., 2018[4]		1:3000/MeOH	

REFERENCES

1. Kim, K. & Rhee, K. The pericentriolar satellite protein CEP90 is crucial for integrity of the mitotic spindle pole. *Cell Sci* **124**, 338–347 (2011).

2. Chevrier, V. *et al* OFIP/KIAA0753 forms a complex with OFD1 and FOR20 at pericentriolar satellites and centrosomes and is mutated in one individual with oral-facial-digital syndrome. *Hum Mol enet* **25**, 497–513 (2016).

3. Kodani, A. *et al* Centriolar satellites assemble centrosomal microcephaly proteins to recruit CDK2 and promote centriole duplication. *li e* **4**, e07519 (2015).

4. Betleja, E., Nanjundappa, R., Cheng, T. & Mahjoub, M. R. A novel cep120-dependent mechanism inhibits centriole maturation in quiescent cells. *li e* **7**, (2018).